Fluid-assisted strain localization in the shallow subcontinental lithospheric mantle

Karoly Hidas, Andrea Tommasi, C. J. Garrido, Jose Alberto Padron Navarta, David Mainprice, Alain Vauchez, Fabrice Barou, Claudio Marchesi

To cite this version:

Karoly Hidas, Andrea Tommasi, C. J. Garrido, Jose Alberto Padron Navarta, David Mainprice, et al.. Fluid-assisted strain localization in the shallow subcontinental lithospheric mantle. Lithos, 2016, 262, pp.636-650. 10.1016/j.lithos.2016.07.038 . hal-01395122

HAL Id: hal-01395122
https://hal.science/hal-01395122

Submitted on 19 Feb 2022

HAL is a multi-disciplinary open access archive for the deposit and dissemination of scientific research documents, whether they are published or not. The documents may come from teaching and research institutions in France or abroad, or from public or private research centers.

L'archive ouverte pluridisciplinaire **HAL**, est destinée au dépôt et à la diffusion de documents scientifiques de niveau recherche, publiés ou non, émanant des établissements d'enseignement et de recherche français ou étrangers, des laboratoires publics ou privés.

Distributed under a Creative Commons Attribution - NonCommercial 4.0 International License

ACCEPTED MANUSCRIPT

Fluid-assisted strain localization in the shallow subcontinental lithospheric mantle

Károly Hidas[1,*], Andréa Tommasi[1], Carlos J. Garrido[2], José Alberto Padrón-Navarta[1], David Mainprice[1], Alain Vauchez[1], Fabrice Barou[1] & Claudio Marchesi[2,3]

1 Géosciences Montpellier, Université de Montpellier & CNRS Place E. Bataillon, 34095 cedex 5, Montpellier, France. karoly.hidas@gmail.com

2 Instituto Andaluz de Ciencias de la Tierra, CSIC & Universidad de Granada, Avenida de las Palmeras 4, 18100 Armilla (Granada), Spain

3 Departamento de Mineralogía y Petrología, Universidad de Granada, Avenida Fuentenueva s/n, 18002 Granada, Spain

** Presently at Instituto Andaluz de Ciencias de la Tierra, CSIC & Universidad de Granada, Avenida de las Palmeras 4, 18100 Armilla (Granada), Spain*

– Manuscript submitted to *Lithos* –

Abstract (257 words)

We report microstructural evidence for fluid-assisted ductile strain localization in a ≤50 m-wide mylonitic-ultramylonitic shear zone in the Ronda peridotite massif, Southern Spain. Strain localization occurred at relatively low pressure (<0.8 GPa) and moderate temperature (750-1000 °C). Initial deformation by dislocation creep resulted in formation of mylonites. Focusing of aqueous fluids in the shear zone favored the activation of dissolution-precipitation creep, resulting in further strain localization. This process is recorded by two generations of

ACCEPTED MANUSCRIPT

ultramylonitic bands composed of fine-grained, well-mixed olivine-orthopyroxene aggregates. Microstructural observations in the ultramylonites suggest alternating dissolution and precipitation of olivine and orthopyroxene, which may be explained by local changes in silica molality of the percolating fluid (disequilibrium and mass transfer at scales > mm). In the mylonites, olivine shows a crystal preferred orientation (CPO) coherent with dominant (001)[100] glide, probably due to the presence of interstitial fluids during deformation. In the ultramylonites, olivine CPO is weak to very weak, consistently with a decreasing contribution of dislocation creep to deformation. In contrast, fine-grained orthopyroxene in both mylonites and ultramylonites display a clear CPO characterized by a [001] maximum normal to the foliation, which is not consistent with dislocation glide in any known slip system for orthopyroxene. We interpret this CPO as formed by oriented crystallization during dissolution-precipitation. In the present study, dissolution-precipitation creep predominates only in small-scale ultramylonite bands due to limited fluid availability and localized dynamic permeability. However, this process may be important in intermediate temperature domains of subduction zones, where it may lead to a feedback between strain localization and fluid transport.

Keywords: strain localization; fluids; dissolution-precipitation creep; shear zone; lithospheric mantle; Ronda Peridotite.

ACCEPTED MANUSCRIPT

Highlights:

- Evidence for a feedback between fluid flow and strain localization in the shallow mantle
- Microstructural evidence for fluid-assisted dissolution-precipitation in peridotites
- Olivine CPO in mylonites indicates (001)[100] glide, probably in presence of fluids
- Evolution from dislocation creep to dissolution-precipitation by fluid focusing
- Abnormal orthopyroxene CPO interpreted as due to oriented crystallization

ACCEPTED MANUSCRIPT

1. Introduction

The processes allowing for mantle peridotites to deform under low temperature conditions (650-1000 °C) are still poorly understood. Deformation experiments on olivine crystals and aggregates under such conditions are characterized by marked hardening, which results under experimental strain rates in transition to a brittle behavior at strains <30% (Demouchy et al., 2013, 2014). Ductile shear zones developed at low temperature are, however, described in many peridotite massifs and ophiolites. Analysis of these data highlights a major role of reactions in the formation of such shear zones (*cf.* Vauchez et al., 2012 and references therein). In many cases, synkinematic reactions occurred under fluid-deficient conditions in response to decompression (*e.g.*, Furusho and Kanagawa, 1999; Newman et al., 1999). However, there is a large body of evidence for a major role of fluids, such as the enrichment in amphibole, chlorite, or antigorite in the low-temperature shear zones of Erro-Tobbio (Vissers et al., 1995) or in amphibole in the ultramylonite bands within the North Lanzo shear zone (Kaczmarek and Tommasi, 2011). These observations suggest localized fluid flow in the shear zones, consistent with data in the lower crust that show ductile shear zones acting as permeable pathways for fluids (*e.g.*, Austrheim, 1987).

Fluid-rock interaction at the grain-scale may have a marked impact on the rheology. Incorporation of protons into defects of the olivine structure is traditionally proposed to result in significant weakening in both the dislocation and diffusion creep regimes (Mei and Kohlstedt, 2000a, b). However, recent diffusion and deformation experiments suggest that the weakening of olivine due to incorporation of protons may have been overestimated (Fei et al., 2013, 2014; Girard et al. 2013). Recent torsion experiments on wet olivine polycrystals also showed a limited strength decrease by factor of 2-3 relative to dry samples, which is associated with the presence

ACCEPTED MANUSCRIPT

of both hydrogen in the olivine structure and water-derived species in grain boundaries or pores (Demouchy et al., 2012). Fluid-saturated grain boundaries may serve as fast intergranular diffusion paths favoring fluid-assisted grain boundary migration (*e.g.*, Urai et al., 1986). They also allow for dissolution-precipitation (pressure-solution) creep, which involves advection of cations and anions by the fluid in response to applied stresses (Rutter, 1976; Spiers et al., 2004).

Dissolution-precipitation creep is a major deformation mechanism in quartz-, plagioclase-, or calcite-rich rocks at low temperature in the shallow to mid-crust (*e.g.*, Wintsch and Yi, 2002; Bestmann et al., 2004), as well as in high-pressure eclogites, serpentinites, phyllites, and schists exhumed from subduction zones (Wassmann and Stöckhert, 2013). It is usually considered as of minor importance in the deformation of peridotites due to the restricted amount of free aqueous fluids in the mantle. Nevertheless, experimental data on the solubility of enstatite and forsterite in nominally pure H_2O at deep crust/uppermost mantle conditions (700-900 °C and 0.4-1.5 GPa; Newton and Manning, 2002) show that the silica solubility is high enough to allow for effective dissolution-precipitation at the scale of tens of centimeters in the laboratory if the fluid composition is not in equilibrium with the solid phases. Thus, if fluids are present and local departures from equilibrium are allowed, dissolution-precipitation creep may be an efficient deformation mechanism in the shallow mantle.

Here we present evidence for ductile strain localization assisted by interstitial fluids in a shear zone in the shallow subcontinental lithospheric mantle of the Ronda massif (Southern Spain). This shear zone is characterized by progressive strain localization, which produced a mylonitic zone with variable width (from a few tens of meters to less than a meter) crosscut by two generations of cm- to mm-wide ultramylonitic bands.

ACCEPTED MANUSCRIPT

2. Mylonitic shear zones in the Ronda Peridotite

The internal zones of the Betic-Rif orogenic belt (westernmost Mediterranean) contain a series of peridotite massifs, which form the largest (>300 km^2) subcontinental lithospheric mantle section exposed on the Earth's surface. In the Ronda Peridotite (Betic Cordillera), fine-grained ultramafic mylonites occur both at the top and at the bottom of the mantle section, recording different stages of the evolution of the massif. Garnet-spinel mylonites occur along a hundred-meter wide zone at the top of the section (Fig. 1, inset) (Van der Wal and Vissers, 1996; Precigout et al., 2013). They are interpreted as accommodating exhumation and cooling of garnet peridotites from 2.4-2.7 GPa (*ca.* 85 km) at 1020-1100 °C to 2 GPa (*ca.* 65 km) at 800-900 °C as a result of thinning of the continental lithosphere in the Oligocene (Garrido et al., 2011). In addition, ductile strain localization in the late stages of the exhumation produced cm- to metric-scale shear zones, which crosscut the plagioclase tectonite domain at the base of the mantle section (Hidas et al., 2013a). These shear zones occur either in plagioclase-bearing pyroxenites, where strain localization is associated with the spinel to plagioclase phase transformation reaction (Hidas et al., 2013b), or in peridotites, as the one studied here. Pyroxenitic and peridotitic shear zones in the plagioclase tectonite domain (Fig. 1) have similar kinematics as indicated by their nearly parallel foliations and lineations and similar sense of shear (Hidas et al., 2013a, b). They are interpreted as coeval to kilometer-scale folding in the Late Oligocene-Early Miocene, which accommodated the final stages of exhumation of the peridotite body and its emplacement in the crust (Hidas et al., 2013a).

ACCEPTED MANUSCRIPT

3. Field structures and sampling strategy

The study area is located in the southwestern part of the Ronda plagioclase tectonite domain (Fig. 1), where plagioclase-bearing and plagioclase-free lithologies coexist. The plagioclase lherzolites show a penetrative high-temperature (high-T) foliation dipping 60-80° to N and a NE-SW trending stretching lineation (Van der Wal and Vissers, 1996; Hidas et al., 2013a). These high-T foliation and lineation are not observed in the more refractory plagioclase-free peridotites, which have coarse-grained microstructures. Both plagioclase-bearing and plagioclase-free peridotites are crosscut by metric to cm-scale shear zones showing a well-developed foliation, which is emphasized in the field by cm- to mm-scale mylonitic and ultramylonitic bands characterized by a marked grain size reduction (Fig. 2). These shear zones have a strike subparallel to that of the high-T foliation in plagioclase tectonites, but a more gentle dip (30-50° to the NNE) (Fig. 1). Within the shear zones, elongated orthopyroxene porphyroclasts denote a NE-SW trending lineation (N25E to N50E), which is subparallel to the lineation in the plagioclase tectonites (Hidas et al., 2013a). Sigmoidal shapes of mylonite lenses within the ultramylonite bands (S-C structures, Fig. 2a) imply top-to-the-SW sense of shear.

Sampling for this study was accomplished along a *ca.* 2 km-long shear zone hosted in coarse-grained peridotites (Fig. 1). This shear zone has a maximum width of 50 meters (Fig. 2a) close to the contact with the crustal Blanca Unit at the base of the massif. It becomes progressively narrower towards the limit between the plagioclase tectonite and the granular spinel peridotite domains (Fig. 1), being <50 cm wide at its termination (Fig. 2b). In its widest section, the shear zone is composed of Mylonite lenses up to few cm wide and tens of cm long, delimited by cm-wide anastomozing Ultramylonite-1 bands (Fig. 2a). The narrow, westernmost section of the shear zone (Fig. 2b) displays a second set of ultramylonite bands (Ultramylonite-

ACCEPTED MANUSCRIPT

2), which have finer grain sizes than Ultramylonite-1. These Ultramylonite-2 bands are subparallel to the Ultramylonite-1 bands, but more planar, locally crosscutting both the Mylonite foliation and the Ultramylonite-1 bands. Their width rarely exceeds 0.5 cm; it is usually < 1 mm.

We sampled the shear zone in three sections along its trend. Samples RK040-RK042 were collected in the widest segment, RK109-RK112 in the intermediate-width segment, and RK167-RK170 at the westernmost tip of the shear zone (Fig. 1). The protolith (RK025-RK027) was sampled a few meters away from the border of the widest segment of the shear zone. All thin sections were cut perpendicular to the foliation in Ultramylonite-1 bands and parallel to the lineation defined by the elongation of the orthopyroxene porphyroclasts in the Mylonite lenses (XZ-section).

4. Modal compositions

Both the protolith and the shear zone are relatively fresh. Serpentinization is very limited, as reflected by the low loss on ignition during whole rock major element analyses (usually < 3 wt.%, Table 1). The protolith is coarse-grained harzburgite or clinopyroxene-poor lherzolite (Table 1) characterized by homogeneously distributed olivine, orthopyroxene, spinel, clinopyroxene and, very rare amphibole (<0.5 %, Fig. 3a). Plagioclase and other accessory minerals are not observed.

The shear zone is also composed by harzburgites, but modal compositions vary between the different microstructural domains. The fine-grained matrix of the Mylonite is enriched in olivine, whereas the ultramylonites have orthopyroxene-rich modal compositions (Fig. 4; Table 1). The ultramylonites also display higher amphibole contents (*ca.* 1.6 %; Table 1). Despite of this heterogeneity, the modal contents calculated based on the whole rock composition of a

ACCEPTED MANUSCRIPT

representative volume of the shear zone, which contains both Mylonite lenses and ultramylonites, do not differ significantly from those of the protolith, except for the enrichment in amphibole (Fig. 4; Table 1).

5. Microstructures

The protolith has a coarse-grained microstructure, characterized by 1-5 mm long olivine and orthopyroxene crystals, which lack any shape-preferred orientation (Fig. 3a-c). Olivine has equant to slightly elongated shapes (aspect ratios ≤1.5; Fig. 3a), undulose extinction, and widely spaced subgrain boundaries (Fig. 3c). Orthopyroxene, clinopyroxene and spinel have irregular shapes (Fig. 3b). The latter two phases may attain up to 1 mm in size. Both ortho- and clinopyroxene show kink bands, undulose extinction and contain exsolution lamellae of clinopyroxene in orthopyroxene and *vice versa* (Fig. 3b-c). Orthopyroxene may also display inclusions of clinopyroxene, olivine, and spinel (Fig. 3b).

The Mylonite lenses have a porphyroclastic microstructure characterized by a bimodal grain size distribution, in which an olivine-rich fine-grained matrix surrounds rare elongated olivine and orthopyroxene porphyroclasts (Fig. 5a-c). Olivine porphyroclasts are seldom larger than a millimeter. Some relict domains indicate that the porphyroclasts were once elongated up to 1 cm in length, but they have been almost fully recrystallized (*cf.* domain delimited by dashed line in Fig. 5a). The olivine neoblasts that compose the matrix have an average equivalent diameter of 180 µm (Fig. 5c, Fig. 6a, d). Both porphyroclasts and neoblasts have a shape-preferred orientation, which defines the foliation and lineation (Fig. 5b-c). They have similar average aspect ratios in the range of 1.8-2.5 (Fig. 6d). Olivine porphyroclasts have undulose extinction (Fig. 5a) and common subgrain boundaries, dominantly at high angle to the elongation

ACCEPTED MANUSCRIPT

of the crystals (Fig. 5c, inset). Subgrains and undulose extinction are less common in the neoblasts.

The size of orthopyroxene porphyroclasts within the shear zone is comparable to those of orthopyroxenes in the protolith, but they are usually elongated, with aspect ratios up to 9 (Fig. 5a-b, Fig. 6d). They are kinked (Fig. 5a) and their grain boundaries are very sutured, with embayments filled by olivine (arrows in Fig. 5c). Orthopyroxene porphyroclasts are also characterized by asymmetric tails of fine-grained, well-mixed olivine-orthopyroxene aggregates (pressure shadow like structures), which extend several cm away from the porphyroclast and often evolve into Ultramylonite-1 bands (Fig. 5b-c). The sigmoidal shape of the porphyroclasts and their tails (Fig. 5b) imply simple shear (top to the SW). Orthopyroxene also occurs in the matrix of the Mylonite lenses as rare small grains (<50 µm on average; Fig. 6a,d) with highly irregular, interstitial-like shapes, which may form film-like structures along olivine-olivine boundaries (Fig. 5c). These small orthopyroxene crystals are more common in the vicinity of the Ultramylonite bands (Fig. 5c,e). Spinel usually occurs in the Mylonite lenses as irregularly shaped or rounded coarse-grained (up to mm) crystals (Fig. 5a-b). In the Mylonite lenses, amphibole and clinopyroxene are rare. When present, they occur as small (<25 µm), irregularly shaped crystals.

The limits between the Mylonite lenses and the Ultramylonite-1 bands are irregular and gradational (Fig. 5c). At the mm-scale, the Ultramylonite-2 bands seem to have sharp planar limits (Fig. 5b), but at the tens of microns scale their limits are also irregular (Fig. 5e). The Ultramylonites have more homogeneous grain size distributions than the Mylonites (Fig. 6). The average grain diameter of the olivine neoblasts decreases drastically to 20-25 µm in Ultramylonite-1 and to 10-15 µm in Ultramylonite-2. The sizes of the fine-grained

ACCEPTED MANUSCRIPT

orthopyroxene in the tails of the porphyroclasts in the Mylonite lenses and in Ultramylonitic bands are significantly smaller than those of olivine in the same domain (Fig. 6). In the matrix of the Mylonite and in the porphyroclasts tails, the mean orthopyroxene equivalent diameter is 40 µm. It is 10 µm in both Ultramylonite-1 and 2 (Fig. 6).

Ultramylonites also differ from the Mylonite by the higher contents in orthopyroxene and amphibole (Fig. 4, Table1) and the more homogeneous phase distribution. Both Ultramylonite-1 and 2 are composed of well-mixed fine-grained olivine and orthopyroxene crystals with irregular, but slightly elongated shapes (aspect ratios up to 5-6, with an average ~2 and shape factors up to 3.5, Fig. 6b-f); their shape-preferred orientation marks the foliation (Fig. 5d-e). Orthopyroxene shows common concave boundaries and form film-like structures along olivine-olivine grain boundaries, more frequently along the faces submitted to compression (Fig. 5d-e). Olivine neoblasts in the Ultramylonite bands may show subgrains, but they are less abundant than in the Mylonite (Fig. 5d-e, insets). The lowest subgrain density is observed in the Ultramylonite-2 bands (Fig. 5e). Spinel is scarce in the ultramylonites. It has a rounded or slightly elongated shape and small grain sizes (<20 µm; Fig. 5d-e). Clinopyroxene and amphibole occur in the Ultramylonite bands as isolated, irregularly shaped, but usually slightly elongated grains (Fig. 5d-e). They have sizes similar to orthopyroxene (<50 µm). Clinopyroxene and amphibole are usually associated and tend to form diffuse bands subparallel to the foliation (Fig. 5d).

ACCEPTED MANUSCRIPT

6. Crystal preferred orientations

6.1. Method

Crystal Preferred Orientations (CPO) were measured by indexing Electron Backscattered Diffraction (EBSD) patterns. CPO maps covering at least 90 % of the thin section surface were obtained for all samples at the SEM-EBSD facility of Géosciences Montpellier (Université de Montpellier, France) using the AZtec data acquisition software (HKL technologies, Oxford Instruments) with a camera setting of 4×4 binning and low gain. Thin-section scale maps were obtained using a JEOL JSM 5600 with a 17 kV acceleration voltage and 24 mm working distance, with grid steps of 14-18 µm for the shear zone samples and 30 µm for the protolith. High-resolution crystal orientation maps were obtained using a CamScan Crystal Probe X500-FEG with 15 kV acceleration voltage, 25 mm working distance, 2 Pa chamber pressure, and grid steps of 0.4-3.5 µm. All major rock-forming phases in the rocks (olivine, enstatite, diopside, chromite and pargasite) were indexed, with a percentage of indexed points in the raw maps exceeding 80 %. Non-indexed points correspond essentially to fractures and grain boundaries. Post-acquisition data treatment was performed following the method summarized in Soustelle et al. (2010).

Mylonitic and ultramylonitic microstructural domains are treated separately after manually defining subsets using the Channel5 software (Oxford Instruments). The grain size and grain shape analyses and the calculation of CPO strength (J-index) were performed using the MTEX toolbox in Matlab (https://mtex-toolbox.github.io/; Bachmann et al., 2010; Mainprice et al., 2014). The J-index, which is the volume-averaged integral of the squared orientation densities (Bunge, 1982), has been derived from orientation distribution functions (ODF) calculated using the mean orientation of each grain with a “de la Vallée Poussin” kernel with a halfwidth of 10°.

ACCEPTED MANUSCRIPT

CPO data were plotted in pole figures based on the mean orientation of each grain to avoid over-representation of large crystals, using the software package by David Mainprice (http://www.gm.univ-montp2.fr/PERSO/mainprice/W_data/CareWare_Unicef_Programs/).

6.2. CPO and misorientations

CPO of olivine and orthopyroxene in the protolith and in Mylonite lenses and Ultramylonite-1 and 2 bands from different outcrops along the shear zone are displayed in Fig. 7. For the protolith we plotted, for reference, both the high-T foliation from the nearby plagioclase tectonites (dotted line) and the orientation of the foliation in the shear zone (dashed line). These two foliations have subparallel strikes but different dips. Due to their low modal contents (Table 1), measured clinopyroxene, amphibole, and spinel CPO are not statistically representative. None of these phases shows strong crystal preferred orientations in any of the microstructural lithotypes.

In the protolith, olivine [100]-axes are concentrated subparallel to the lineation and [010]-axes show a point-like maximum normal to the high-T foliation in the plagioclase tectonites. In the Mylonite lenses and Ultramylonite-1 bands, olivine [100]-axes are aligned subparallel to the lineation and the [001]-axes tend to be normal to the foliation of the shear zone. Due to the anastomozed character of the foliation in the shear zone (*cf.* Figs. 2 and 5), in some samples, as in RK-109, the olivine CPO is at an angle to the average foliation and lineation in the shear zone, which is used as the reference for plotting the CPO data. It is however coherent with the local orientation of the foliation and lineation. In Ultramylonite-2 bands the olivine CPO is almost random, but [100]-axes tend to form a weak girdle at an angle to the foliation, and weak maxima of [010]- and [001] axes are present subnormal to the lineation, but oblique to the foliation plane.

ACCEPTED MANUSCRIPT

The strength of the CPO may be quantified by the J-index, which ranges from unity for a random fabric to infinity for a single crystal. Most natural peridotites show olivine J-indices between 2 and 20, with a predominance of J-indices ≤ 6 (>75 % of the analyzed samples, *cf.* Tommasi and Vauchez, 2015). The protolith has weak olivine CPO (J-index = 2.3). Olivine CPO is strong in the Mylonite lenses (J-indices of 5-8.6), but very weak in the Ultramylonite bands (J-indices <1.5; Fig. 7).

In the protolith, orthopyroxene has a weak CPO, which is characterized by a tendency for alignment of [100]-axes at high angle to the foliation and of [001]-axes subparallel to the foliation plane. Due to the relatively low amount of orthopyroxene porphyroclasts in the Mylonite (*cf.* Fig. 5a-b) the CPO is statistically not representative, but the porphyroclasts (not shown in Fig. 7) are usually elongated with [001]-axes subparallel to the lineation and [100]-axes perpendicular to the foliation. The CPO of the fine-grained orthopyroxenes in all domains of the shear zone (Mylonite lenses, Ultramylonite-1 and 2 bands) is markedly different. Although weak (J-index <2), it is characterized by a clear point maximum of [001]-axes perpendicular to the foliation and by a girdle distribution of [100]- and [010]-axes subparallel to the foliation plane with a weak concentration of [100]-axes subparallel to the lineation. The similarity of the fine-grained orthopyroxene CPO in all three domains is noteworthy. Analysis of Fig. 7 also highlights that the distribution of the [001]-axes of fine-grained orthopyroxene mimics that of olivine [001]-axes with a *ca.* 20° obliquity in both the Mylonite lenses and Ultramylonite-1 bands. This relation is not verified in the Ultramylonite-2 bands, because the olivine CPO in these bands is almost random.

In the protolith, the rotation axes accommodating low-angle (2-15°) misorientations within olivine crystals have <0vw> orientations, whereas in orthopyroxene intracrystalline

ACCEPTED MANUSCRIPT

misorientations are accommodated mainly by rotations around [010] (Fig. 7). In case of orthopyroxene porphyroclasts in the Mylonite lenses, the intracrystalline misorientations are similar to those of the protolith. Different rotation axes across subgrain boundaries are, however, observed in all fine-grained domains in the shear zone (Fig. 7). In olivine neoblasts from Mylonite and Ultramylonite-1 bands, low-angle misorientations are accommodated mainly by rotations around [010]. In olivine from Ultramylonite-2 bands, rotations around [100] are also observed. Fine-grained orthopyroxenes in both the Mylonite lenses and Ultramylonite bands display very low intracrystalline misorientations. However, when present, these misorientations result dominantly from rotations around [001] (Fig. 7).

7. Major element geochemistry

7.1. Mineral chemistry

Mineral compositions were measured using a CAMECA SX100 electron microprobe (EPMA) equipped with 5 spectrometers at Géosciences Montpellier (France). Analyses were carried out using an accelerating voltage of 20 kV, a beam current of 10 nA, and 1 µm beam size with counting times of 10-20 s. Natural and synthetic silicate and oxide standards were used for calibration and ZAF correction was applied. Data are shown in Supplementary Table S1.

Olivine is forsterite-rich (Mg# = 0.91-0.92) and has NiO contents of 0.37-0.48 wt. %. It does not show any systematic variation in composition among the different microstructures, nor as a function of grain size within the Mylonite lenses or Ultramylonite bands or relative to the surrounding harzburgites (Hidas et al., unpublished data). Cr and Al contents in ortho- and clinopyroxenes decrease from the porphyroclasts' cores to the rims. Cr and Al contents are also low in the small grains in the Mylonite lenses and Ultramylonite bands. The lowest values occur

ACCEPTED MANUSCRIPT

in a layer <20 µm wide at the porphyroclasts edges and in the smaller crystals of the Mylonite lenses and Ultramylonite bands. Amphiboles were analyzed only in the Ultramylonite bands; they have pargasitic compositions with high Cr_2O_3 content (1.07-2.12 wt.%) and Al_2O_3 concentrations (max. 12.4 wt.%). There is no systematic variation between the compositions of fine-grained orthopyroxenes or amphiboles from Ultramylonite-1 and 2 bands.

7.2. Geothermometry

Temperatures are calculated using the Cr and Al content in orthopyroxene thermometer (Cr-Al-Opx) of Witt-Eickschen and Seck (1991) and the Ca content in orthopyroxene thermometer (Ca-in-Opx) of Brey and Köhler (1990) (Fig. 8). The estimated uncertainty of these thermometers given by the authors is ±16 °C. For the Ca-in-Opx method, temperatures are estimated for a pressure of 0.8 GPa, which is the pressure of spinel to plagioclase phase transformation reaction associated with strain localization in nearby pyroxenitic shear zones with similar kinematics (Hidas et al., 2013b). This allows straightforward comparison of temperatures without the need of considering the effect of pressure on the calculations.

Figure 7 summarizes the equilibrium temperatures obtained using both thermometers based on the compositions of orthopyroxenes within the shear zone. They are consistent, though the Ca in orthopyroxene method predicts higher equilibrium temperatures for the fine grained pyroxenes (~50 °C) and, in some cases, lower equilibrium temperatures for the porphyroclasts cores (up to 100 °C). To analyze the variation in equilibration conditions between the different microstructural domains, for the sake of simplicity, we focus on the results of the $T_{Cr\text{-}Al\text{-}Opx}$ method. Cores of orthopyroxene porphyroclasts in the Mylonite lenses give temperatures of 850-1000 °C, which overlap with the pre-kinematic conditions in the nearby pyroxenitic shear zone

ACCEPTED MANUSCRIPT

(Hidas et al., 2013b). These temperatures are minimum estimates due to exsolution of secondary clinopyroxene (and spinel) in orthopyroxenes. Rim compositions record cooling down to 785 °C (785-975 °C). The lowest temperatures in the porphyroclasts' rims overlap with the highest temperatures estimated for neoblasts in the Mylonite lenses (700-830 °C), Ultramylonite-1 bands (680-830 °C) and Ultramylonite-2 bands (680-780 °C). They are also consistent with post-kinematic conditions estimated for the nearby pyroxenite shear zone (750-800 °C; Hidas et al., 2013b). Temperatures calculated for the outmost edge of orthopyroxene porphyroclasts show a higher dispersion, ranging between 670-910 °C. They overlap with the entire range of temperatures obtained from the compositions of the small grains in the Mylonite and Ultramylonite-1 and 2 bands.

All calculated values except one outlier (obtained from the composition of the outmost edge of a porphyroclast) plot above the chlorite stability field at 0.8 GPa, in agreement with the absence of this mineral phase in the samples. These data suggest that the deformation producing the shear zone took place under decreasing temperature conditions, starting with formation of the Mylonite at >900 °C down to development of the Ultramylonite-2 bands at temperatures of 800-750 °C. However, in spite of this internal consistency, the temperature variation among the different microstructural facies may also result from differences in the diffusion closure temperatures due to the variations in grain size. Indeed, based on diffusion data for orthopyroxene (Cherniak and Dimanov, 2010 and references therein) and on published exhumation rates of the Ronda massif (100 to 300 °C/Ma; Precigout et al., 2013 and references therein), we estimate that average closure temperature of an orthopyroxene grain with 15 µm diameter is approximately 735-760 °C and that it increases to 780-805 °C for a 30 µm grain diameter. These values are similar to the temperatures obtained based on the chemistry of the

ACCEPTED MANUSCRIPT

fine-grained orthopyroxenes in the Ultramylonite bands. The lower temperatures obtained for the ultramylonites might therefore record more efficient post-kinematic re-equilibration during the last stages of exhumation and cooling of the massif.

Thus, although the progressive grain size refinement and strain localization that characterizes the shear zone corroborates deformation under retrograde conditions, we cannot use pyroxene thermometry to constrain with precision the temperature conditions prevailing during the different stages of the evolution of the shear zone. The latter are nevertheless bracketed by the amphibole-out and the chlorite-in reactions (Fig. 8). If, based on the similarity of their kinematics, we hypothesize that the shear zone studied here formed during the same deformation episode as the shear zones crosscutting the pyroxenite layers studied by Hidas et al. (2013b) – in which shearing catalyzed the spinel-plagioclase phase transition reaction at *ca.* 0.8 GPa – we may further constrain the temperature range to 750-1000 °C (Fig. 8).

8. Discussion

8.1. Relationships between the protolith deformation and the shear zone

The coarse-grained microstructures, the well-developed subgrains in olivine and kinks in orthopyroxene (Fig. 3), and the CPO of olivine and orthopyroxene in the protolith are consistent with deformation by dislocation creep with dominant activation of {0kl}[100] slip systems in olivine and (100)[001] in orthopyroxene (Fig. 7). This microstructure and CPO suggest deformation under low stress, high temperature (>1000 °C), low pressure, and dry conditions (*cf.*, Carter and Avé Lallemant, 1970; Durham and Goetze, 1977; Mainprice et al., 2005; Karato 2008; Jung et al., 2010; Demouchy et al. 2014). Olivine and orthopyroxene CPO in the plagioclase-free coarse-grained peridotites that host the shear zone (Fig. 7) are coherent with the

ACCEPTED MANUSCRIPT

foliation and lineation of plagioclase tectonites (Fig. 1; Van der Wal and Vissers, 1996), indicating that all rock types that composed the plagioclase tectonite domain were submitted to the same pervasive high-temperature, low pressure deformation event.

Microstructural and petrological observations indicate that the shear zone formed under low pressure (*ca.* 0.8 GPa) and intermediate temperature (750-1000 °C) conditions via three stages of strain localization associated with increasing grain size reduction: formation of the Mylonite lenses and of the two generations of Ultramylonite bands (Ultramylonite-1 and 2). The shear zone kinematics is rather similar to those of the surrounding coarse-grained peridotites: lineations have the same orientation and foliation planes only differ by their shallower dips (Fig. 1, Fig. 7). This similarity may be interpreted as indicating that the coarse-grained peridotites outside the shear zone record the earlier stages of the same deformation event, pre-strain localization. An alternative interpretation would be that these rocks record an older, unrelated deformation and that their structure influenced the development of the shear zone. The data collected in the present study does not allow discriminating between these two hypotheses, but the marked change in the microstructure, in particular the marked grain size reduction between the protolith and the Mylonites suggest a gap in deformation conditions (significantly higher work rates in the shear zone, indicating either lower temperatures or higher strain rates).

8.2. Mylonites: the initial stages of strain localization

The porphyroclastic microstructure of the Mylonite lenses is characterized by highly elongated olivine grains and orthopyroxene porphyroclasts (Fig. 5a-b, Fig. 6d), with frequent intracrystalline deformation features (such as undulose extinction, subgrains, and kink bands; Fig. 5a, c) surrounded by a matrix of recrystallized olivine crystals with an average grain size of

ACCEPTED MANUSCRIPT

180 µm (Fig. 6a). This microstructure is consistent with deformation by dislocation creep with dynamic recrystallization leading to significant grain size reduction of olivine. The almost total recrystallization of olivine and the asymmetry of the microstructure (Fig. 5) support deformation up to high shear strains. In contrast, orthopyroxenes are only elongated when well oriented for glide dislocation on the (100)[001] and do not show any clear evidence of recrystallization. Such microstructures are consistent with deformation under moderate to high stress conditions, consistent with the equilibrium temperatures estimated based on the orthopyroxene core compositions (850-1000 °C). Moderate stresses of 20-25 MPa are indeed obtained using the average olivine recrystallized grain size and the piezometers of Karato et al. (1980) and Van der Wal et al. (1993).

The microstructures in the Mylonites are similar to those observed in shear zones developed under dry conditions and similar temperatures in other peridotite massifs, like Turon de Tecouère (Newman et al., 1999) and Beni Bousera (Frets et al., 2014), or in the garnet-spinel mylonites from the top section of the Ronda massif (Soustelle et al., 2009; Precigout et al., 2013). However, the olivine CPO in the Mylonites differs from those described for the mylonitic domains of these shear zones by its unusual concentration of [001] axes normal to the foliation (Fig. 7). The olivine CPO in the Mylonites is also markedly different from the one in the protolith (Fig. 7). This difference rules out formation of the CPO by reactivation of the protolith fabric as proposed for shear zones in the Oman ophiolite (Michibayashi and Mainprice, 2004) and in the Red Hills massif (Webber et al., 2008). The olivine CPO in the Mylonites suggests dominant activation of the (001)[100] system, instead of the (010)[100], which is the most common slip system in olivine in both the lithospheric and asthenospheric mantle. The predominance of [010] rotation axes accommodating misorientations across subgrain boundaries

ACCEPTED MANUSCRIPT

(that is, intracrystalline misorientations <15°) in olivine in the Mylonite lenses (Fig. 7) indicates a high density of dislocations of the (001)[100] system preserved in the subgrain boundaries, corroborating its activation during deformation.

The (001)[100] slip system has been proposed to be dominantly activated during deformation of olivine with water contents of 200-1000 H/10^6Si (12-60 wt ppm H_2O), moderate stresses (400 MPa) and pressures (2 GPa), and high temperature (Katayama et al., 2004). Due to the small grain sizes and serpentinization along grain boundaries and fractures, water contents in olivine could not be measured by FTIR, not even for the rare porphyroclasts in the Mylonite lenses. Yet, the water solubility in olivine at the low-pressure and relatively low-temperature conditions inferred for the shear zone activity is very low. At 0.8 GPa and 750-1000 °C, it ranges from 11 to 38 ppm based on the extrapolation of experimental data in simple systems (MgO-SiO_2-H_2O; Bali et al., 2008). Thus water saturation is needed to explain the change in dominant slip plane by incorporation of water in the olivine structure.

Olivine CPO characterized by concentration of [001] normal to the foliation plane has been observed in dunite and harzburgites from the shallow mantle section (<2 km from the Moho) of the Talkeetna arc, where it was attributed to high hydroxyl concentrations in olivine (Mehl et al., 2003). A similar interpretation had also been suggested to explain such olivine CPO in moderate temperature (~900 °C), hydrated domains of a shear zone at the Moho Transition Zone of the Oman ophiolite (Michibayashi and Oohara, 2013). Olivine CPO characterized by concentration of [001] normal to the foliation plane was also described in dunitic bands from ophiolites, where deformation occurred in presence of Si-undersaturated melts (*e.g.*, Cassard, 1980; Suhr, 1993; Tommasi et al., 2006). In the studied shear zone, deformation in presence of melts may be ruled out based on the lack of major changes in chemistry (Table 1) and by the equilibrium

ACCEPTED MANUSCRIPT

temperatures <1000 °C (Fig. 8). In contrast, as discussed below, evidence for the presence of aqueous fluids in the shear zone is widespread. We propose therefore that the observed change in dominant slip system in olivine is associated with presence of limited amounts of aqueous fluids during deformation.

Independent evidence for presence of fluids during the formation of the Mylonites can be derived from the analysis of the microstructures. The sinuous boundaries of the orthopyroxene porphyroclasts (*cf.* high shape factors of porphyroclasts in Fig. 6a) with embayments filled by olivine (Fig. 5c) imply replacement reactions of orthopyroxene by olivine involving silica mass transfer at the 10-100s of µm scale. Milke et al. (2009, 2013) observed similar features (which they called bulging) in orthopyroxene growth experiments at olivine-quartz reaction interfaces at 700-950 °C and 1.9 GPa that they interpreted as recording the presence of fluids. Synkinematic mass-transfer, but with even longer characteristic distances (≥ mm), is also needed to explain the formation of the asymmetric tails in pressure shadow configurations composed of well-mixed olivine-orthopyroxene aggregates, which extend up to several cm away from the orthopyroxene porphyroclasts, often evolving into Ultramylonite-1 bands (Fig. 5b-c). The spatial relation between the 'corrosion' on the orthopyroxene porphyroclasts and the olivine-orthopyroxene tails suggests that both features are genetically related. As discussed below (Section 8.4), solid-state diffusion is too slow to account for effective mass-transfer at these scales, implying advection of matter by fluids.

One point that cannot be constrained based on the microstructural data observations is whether strain localization leading to formation of the mylonites started under dry or wet conditions. The olivine CPO indicates nevertheless that most of the strain has been accumulated in presence of limited amounts of fluids, suggesting fluid focusing in the active shear zone.

ACCEPTED MANUSCRIPT

8.3. Ultramylonite bands: Feedbacks between strain localization and fluids focusing

The finer grain sizes (Fig. 6), lower density of subgrain boundaries in olivine (Fig. 5c-e, inset), and increasing dispersion of the olivine CPO (Fig. 7) clearly point to a decreasing contribution of dislocation creep to the deformation in the Ultramylonite bands. On the other hand, the extensive and pervasive phase mixing, the sinuous olivine-orthopyroxene grain boundaries, and, most importantly, the interstitial or film-like shapes of orthopyroxenes (Fig. 5d-e) imply an increasing contribution of dissolution-precipitation creep.

Deformation by dissolution-precipitation creep may also account for the CPO of the fine-grained orthopyroxenes (Fig. 7), which is difficult to explain otherwise. In contrast to olivine, neither the pattern nor the intensity of the CPO of the fine-grained orthopyroxenes vary significantly between the Mylonite lenses and Ultramylonite bands (Fig. 7). This CPO, which is characterized by a concentration of [001] axes normal to the foliation, cannot have formed by dislocation glide, since TEM observations in orthopyroxene show almost solely dislocations with [001] Burgers vectors (*e.g.*, Naze et al., 1987; Steuten and Van Roermund, 1989). In a CPO formed by dislocation glide, the [001] axes should therefore align parallel to lineation, as usually described in deformed mantle rocks (Soustelle et al., 2010; Frets et al., 2014).

Orthopyroxene CPO with [001] axes aligned normal to the foliation were nevertheless described in orthopyroxene-impregnated dunites of the Bay of Islands ophiolite (Suhr, 1993) and in ultramylonitic shear zones of the Othris peridotite massif (Dijkstra et al., 2002). In both cases this anomalous orthopyroxene CPO was interpreted as formed due to syntectonic melt-facilitated precipitation reaction. Similarly, we propose that the unusual CPO of the orthopyroxene neoblasts in the Mylonites and Ultramylonites results from oriented synkinematic crystallization

ACCEPTED MANUSCRIPT

via dissolution-precipitation processes (*e.g.*, Wassmann and Stöckhert, 2013 and references therein). This interpretation is corroborated by the correlation between the shape-preferred orientation (SPO) and the CPO of the fine-grained orthopyroxenes (*i.e.,* elongated parallel to [100] and flattened parallel to [001], illustrated by comparison between Figs. 5 and 7), as expected for oriented growth.

The synkinematic nature of the dissolution-precipitation reactions in both Ultramylonite-1 and 2 bands is attested by the elongation and alignment of the fine-grained orthopyroxene crystals parallel to the foliation or to the shear plane (Fig. 5d-e). In addition, the preferential occurrence of film-like orthopyroxene crystals along olivine boundaries parallel to the foliation, that is, in compressional sites, rules out crystallization in voids or cavities opened by grain boundary sliding (Chokshi and Langdon, 1987). In-situ deformation of octachloropropane in the grain boundary sliding regime shows indeed that cavities develop preferentially along boundaries at low angle to the shortening direction (Ree, 1994). Dissolution-precipitation creep may, however, produce the observed microstructure if fluid flows dominantly parallel to the shear plane. Higher fluid fluxes along the faces parallel to the shear plane and the foliation will control the triggering of the crystallization reaction. The elongated shapes of the crystals suggest nevertheless that further growth occurred by continued precipitation on the extensional faces of orthopyroxene neoblasts.

In conclusion, we propose that the change in microstructures and CPO of olivine and orthopyroxene from the Mylonite lenses to the Ultramylonite bands records a decreasing contribution of dislocation creep and increasing contribution of dissolution-precipitation creep, the Ultramylonite-1 bands representing an intermediate stage. This change in dominant deformation mechanism is accompanied by progressive strain localization. Feedbacks between

ACCEPTED MANUSCRIPT

deformation and permeability probably resulted in focusing of the fluid flow and by consequence in more effective deformation, favoring strain localization up to the formation of the very thin Ultramylonite-2 bands.

8.4. Diffusion-precipitation creep vs. solid-state diffusion-accommodated grain boundary sliding

Diffusion-assisted grain boundary sliding has been often proposed to account for mass-transfer and phase mixing (*e.g.*, Warren and Hirth, 2006). However, the sinuous, interpenetrating shapes of olivine and orthopyroxene interphase boundaries in the Mylonites and Ultramylonites (Fig. 5) are not compatible with grain boundary sliding. Moreover, when starting from a coarse-grained material as the protolith of the studied shear zone, phase-mixing by grain boundary sliding requires an initial grain size reduction by dynamic recrystallization. There is clear evidence in the Mylonites for grain size reduction of olivine by this process (Fig. 5a-c). However, orthopyroxenes do not show any sign of dynamic recrystallization by neither subgrain rotation (no core and mantle structure, only a few kinks are observed within the porphyroclasts), nor bulging (grain boundaries are sinuous, but the embayments are filled by olivine) (Fig. 5a-c). Last but not least, grain boundary sliding should either disperse the CPO of both olivine and orthopyroxene, or produce weak orientations of both, if they display anisotropic shapes (Wheeler, 2009). In the studied shear zone the olivine CPO is strongly dispersed in the fine-grained domains, but the fine-grained orthopyroxenes show a clear CPO with similar intensity in all domains from the Mylonite lenses to the Ultramylonite bands (Fig. 7). Moreover, the olivine and the orthopyroxene CPO in the studied shear zone are markedly different from those formed in experiments where diffusion- or dislocation-accommodated grain boundary sliding have been

ACCEPTED MANUSCRIPT

proposed to dominate (e.g. Cooper and Sundberg, 2008; Hansen et al. 2011; Miyazaki et al. 2013).

In summary, 'dry' diffusion- or dislocation-accommodated grain boundary sliding cannot explain neither the microstructures nor the CPO in the studied shear zone. This conclusion is consistent with recent experiments especially designed to test for feasibility of long wavelength phase mixing by grain boundary sliding in an aggregate composed of coarse orthopyroxenes embedded in an olivine matrix, which show that such mixing is limited to a 1-2 grains-wide layer at the border of the porphyroclasts (Linckens et al., 2014). Dry mechanical phase mixing is also at odds with the predictions of numerical models of deformation of two-solid phase aggregates (Dabrowski et al., 2012) and with experiments in which superplasticity (diffusion-accommodated grain boundary sliding) predominates (Hiraga et al., 2013), which show phase segregation in initially well-mixed aggregates.

Under fluid-absent conditions, mass-transfer may also be accommodated by solid-state diffusion. Sinuous olivine-orthopyroxene phase boundaries have been observed in high temperature (1200 °C) dry deformation experiments on fine-grained olivine-orthopyroxene aggregates (final grain sizes are <10 μm), in which interface-reaction-controlled diffusion creep dominated (Sundberg and Cooper, 2008). However, the length scale of the reactions (*i.e.,* formation of olivine at the expenses of orthopyroxene and vice-versa) in these experiments is at most a few microns, that is, mass-transfers occur at the scale of preexisting olivine-orthopyroxene grain boundaries in an initially well-mixed aggregate. This observation is consistent with the low atomic diffusivities in olivine. For instance, Si diffusion rates in olivine at 1000 °C range from 3.44×10^{-22} m^2/s (hydrous olivine; Costa and Chakraborty, 2008) to 3.74×10^{-24} m^2/s (dry forsterite; Fei et al., 2012). Even considering the highest diffusion rate, the

ACCEPTED MANUSCRIPT

characteristic diffusion length is *ca.* 100 µm in 1 million year, which is already a too long time span for the continuous functioning of a small shear zone like the one studied here.

Mass transport at the ≥cm length scales observed in the studied shear zone is nevertheless possible in presence of fluids. Experimental investigation of orthopyroxene growth at olivine-quartz reaction interfaces suggests that the presence of a free fluid phase enhances the kinetics of mineral replacement by 5 to 7 orders of magnitude with respect to dry conditions at the same temperature (Milke et al., 2007, 2009). The formation of an interconnected fluid network results in a sudden and significant reduction in the solid diffusion distance, as it then corresponds to the distance to the closest wetted boundary (Takei, 1998; Holtzman, 2016). Dissolution-precipitation during deformation in presence of a fluid phase may thus explain the corrosion of orthopyroxene porphyroclasts (*cf.* high shape factors of porphyroclasts in Fig. 6a), their partial replacement by olivine (Fig. 5c), and the crystallization of small orthopyroxene grains within the orthopyroxene tails (Fig. 5b-c) and Ultramylonite bands (Fig. 5d-e).

Very similar microstructures – irregularly-shaped orthopyroxene porphyroclasts with olivine embayments and intermixed fine-grained olivine-orthopyroxene aggregates with elongated, flaser-like orthopyroxenes crystallized along olivine grain boundaries – and the same abnormal orthopyroxene CPO as those observed in the presently studied shear zone have been described in the Othris (Dijkstra et al., 2002) and Table Mountain (Suhr, 1993) ophiolites. In both studies, these features were explained as resulting of melt-mediated dissolution-precipitation processes. Given the low temperatures inferred for the functioning of the shear zone (Fig. 8) and the similarity in major element compositions between the protolith and the shear zone (Table 1), we propose that aqueous fluids and not melts are responsible for the efficient mass-transfer in the studied rocks.

ACCEPTED MANUSCRIPT

An effective role of dissolution-precipitation by aqueous fluids has also been proposed to explain the formation of olivine-orthopyroxene well-mixed fine-grained aggregates in the Anita Bay peridotite (Czertowicz et al., 2016). However, their model differs from the present one by proposing that the orthopyroxene neoblasts precipitate from a fluid into pores (cavities) opened between olivine grains during deformation by grain boundary sliding. As discussed in section 8.3, the preferential occurrence of film-like orthopyroxene crystals along olivine boundaries parallel to the foliation (Fig. 5c-e), that is, in compressional sites, rules out crystallization in voids or cavities opened by grain boundary sliding in the presently studied shear zone.

8.5. Is dissolution-precipitation creep physically viable in peridotites?

Dissolution-precipitation creep requires (i) the existence of a free fluid phase along grain boundaries and/or filling a transient porosity produced during fluid-mineral interaction, (*e.g.* Putnis, 2015 and references therein), (ii) a finite solubility of the oxide components in the fluid phase, and (iii) a physicochemical gradient. Recent experiments of Milke et al. (2009, 2013) at 700-950 °C and 1.9 GPa suggest that fluid saturation can be achieved even at extremely low water concentrations in MgO-SiO_2-H_2O simple chemical systems, representative of the mantle. In these experiments, where mass transfer is triggered by a local chemical gradient resulting from the contact between an olivine and a quartz crystal, the existence of only 20 wt. ppm of excess water in the form of a free fluid phase (filling pores of 2-5 µm in length) is enough to produce *ca.* 20 µm wide orthopyroxene rim in 72 h, indicating reaction rates equivalent to those observed in systems with several thousands of ppm water. In natural systems, additional components, such as CaO, Al_2O_3, and Na_2O, will result in the crystallization of hydrous phases, such as amphiboles, at the aforementioned pressure and temperature conditions (Fig. 9 and also

ACCEPTED MANUSCRIPT

Green et al., 2010), limiting the free water content. For a peridotitic composition, fluid saturation is reached at 1.0-1.4 wt.% amphibole content at the pressure and temperature conditions estimated for the shear zone (Fig. 9). This value is in excellent agreement with the modal amount of amphibole observed in the shear zone, particularly in the Ultramylonites (1.0-1.6 area %; Fig. 5; Table 1). Note that once the system reaches saturation (*i.e.*, the maximum amount of amphibole is formed), further fluid percolation will not result in increase of amphibole content, but in free fluid. It is also worth to note that at pressures higher than 3 GPa and lower than *ca.* 0.4 GPa, amphibole is no longer stable (Fig. 9) and dissolution-precipitation creep can be activated at very low water concentrations, similar to those in the experiments.

Available experimental data on aqueous fluids coexisting with olivine and pyroxene at deep crust/upper mantle conditions (700-900 °C and 0.4-1.5 GPa, Zhang and Frantz, 2000; Newton and Manning, 2002) indicate that under the conditions inferred for the functioning of the shear zone, the molality of aqueous SiO_2 in the fluid ranges from 0.16 to 0.5 mol/kg. These values are only four times lower than the SiO_2 solubility in quartz-saturated fluids (Manning, 1994) or in fluids buffered by albite+paragonite+quartz (Manning et al., 2010). Field and experimental evidence for dissolution-precipitation creep has been well documented in quartz-rich and feldspar-rich lithologies under fluid saturation conditions (*e.g.,* Tullis et al., 1996; Stöckhert et al., 1999; Menegon et al., 2008). By analogy to these systems, we conclude that SiO_2 solubility in fluids buffered by olivine and orthopyroxene is enough to promote effective mass transfer. This conclusion is corroborated by the experiments of Milke et al. (2009, 2013) and by natural observations suggesting dissolution (Padrón-Navarta et al., 2010a) or crystallization of orthopyroxene (e.g., McInnes et al., 2001; Soustelle et al., 2010) in peridotites by aqueous fluids with small amounts of dissolved silicates.

ACCEPTED MANUSCRIPT

The third requirement that needs to be addressed is the existence of local physicochemical gradients necessary to produce a heterogeneous fluid composition and therefore effective mass transfer. It can be envisaged that the low permeability of peridotites, even under dynamic conditions, will result in a sluggish fluid flow. Under these conditions the composition of the fluid will be locally controlled by the minerals in direct contact with the fluid leading to local disequilibrium and to spatial variations in the silica concentration. These changes in the percolating fluid will allow for alternating dissolution and precipitation of olivine and orthopyroxene, accounting for the microstructural observations, which point to both crystallization of olivine at the expense of orthopyroxene (aqueous SiO_2 increasing in the fluid) – *e.g.,* the presence of olivine in the embayments of the orthopyroxene porphyroclasts (Fig. 5c) – and the crystallization of orthopyroxene at the expense of olivine (aqueous SiO_2 decreasing in the fluid) in the pressure shadows and tails of orthopyroxene porphyroclasts, as well as in the Ultramylonite bands (Fig. 5c-e). An alternative explanation is that the fluid composition is heterogeneous due to variations in the stress field at the grains' scale (*e.g.*, Wheeler, 1987). This effect will be enhanced at relatively low-pressure conditions (<0.8 GPa) where the SiO_2 solubility in fluids is more dependent on local pressure variations than in temperature (*cf.* Fig. 6 in Newton and Manning, 2002).

In experiments, crystallization of orthopyroxene at the expenses of olivine results in compositional gradients, in particular, enrichment in Ni in olivine in the vicinity of the reaction zone (Milke et al., 2011). Such gradients are not observed in the Mylonites and Ultramylonites. We have shown in Section 7.2 that solid state re-equilibration in the fine-grained peridotites that compose the shear zone may have reset even the elements with the slowest diffusion coefficients in orthopyroxene, such as Cr. Given that the diffusion of Ni in olivine is orders of magnitude

ACCEPTED MANUSCRIPT

faster (*e.g.,* Petry et al., 2004) than that of Cr in orthopyroxene (Cherniak and Dimanov, 2010 and references therein), the current lack of compositional gradients in the studied shear zone may be explained by solid-state re-equilibration coupled to the high amount of olivine as Ni reservoir (Fig. 4) and the more diffuse spatial distribution of reactions (*cf.* Fig. 5) in nature than in the experiments.

8.6. Where in the upper mantle may dissolution-precipitation creep occur?

The conditions at which dissolution-precipitation may be active in the upper mantle are very restrictive. This process requires significant amounts of free aqueous fluids and, hence, the presence of a fluid-source. The existence of free aqueous fluids in the mantle is also limited by the crystallization of hydrous minerals, such as chlorite that forms at temperatures below *ca.* 700-750 °C (Fig. 9) (*e.g.*, Vissers et al., 1995; Padrón-Navarta et al., 2010b) and by the onset hydrous melting (*ca.* 1000-1100 °C; Green, 1973).

It is therefore difficult to envisage a process leading to large fluxes of aqueous fluids through the subcontinental lithospheric mantle. However, the latest stages of exhumation of the Ronda peridotite massif involve kilometer-scale folding and subsequent shearing of a previously highly attenuated continental lithosphere in response to back-arc basin inversion (Hidas et al., 2013a, 2015). The studied shear zone formed in the hinge zone of this large-scale fold (Fig. 1 and also Hidas et al., 2013a). In such a setting, limited amounts of fluids might have been released by dehydration of crustal units overthrust by the peridotites and channeled by pressure gradients in the hinge zone of the fold. This model is corroborated by the geometry of the shear zone, which suggests that it propagated upwards from the vicinity of the contact with the crustal units towards the center of the massif (Fig. 1). The presence of crustal units beneath the

ACCEPTED MANUSCRIPT

peridotites is further supported by the Sr-Nd-Pb radiogenic isotopic signature of late high-Mg pyroxenite dikes that crosscut the Ronda peridotites (Marchesi et al., 2012), which suggests that they formed by fluid-flux melting of lower crustal granulites similar to those that currently overlie the massif (Varas-Reus et al., in prep).

The conditions allowing for the existence of significant amounts of free aqueous fluids may nevertheless be achieved locally in the mantle atop a subduction zone, in a domain delimited by the serpentinite and chlorite stability and the wet solidus (*e.g.*, Van Keken et al., 2002). If enough free fluids are present, dissolution-precipitation creep may allow deformation of mantle rocks in these rather cold domains of the mantle at lower stresses than dislocation creep. It may therefore be a key process allowing for deformation and maybe partial decoupling of the plates between the deeper, higher temperature domains of the wedge and shallower, serpentine-lubricated fault zones. If active, dissolution-precipitation creep would imply in feedback between deformation and fluids transport and, hence, in highly heterogeneous deformation in the shallow mantle wedge. Association of highly localized deformation and the very weak olivine CPO produced by dissolution-precipitation creep may also provide an explanation for the very weak seismic anisotropy usually recorded in the fore-arc domains of subduction zones (delay times <0.5 s, *e.g.,* Long and Silver, 2008; Di Leo et al., 2012).

9. Conclusions

Analysis of the compositions, microstructures and crystal preferred orientations from a shear zone in the Ronda massif (Southern Spain) consistently points to fluid-assisted ductile strain localization in the shallow mantle lithosphere. This shear zone is 50 m wide close to the contact with the crustal units, but <50 cm in its termination, close to the limit with the granular spinel

ACCEPTED MANUSCRIPT

peridotite domain. It is composed of Mylonite lenses surrounded by mm-scale Ultramylonite bands, which are composed of fine-grained (average grain sizes <20 μm) well-mixed olivine-orthopyroxene aggregates with sinuous interphase grain boundaries. The microstructures in Mylonite lenses, such as the elongated porphyroclasts of olivine and orthopyroxene and the high density of subgrains in olivine, imply that dislocation creep predominated in the early stages of development of the shear zone. Channeling of aqueous fluids in this evolving shear zone is supported by (1) the unusual olivine CPO, which indicates dominant activation of (001)[100] glide; (2) the corroded shapes of orthopyroxene porphyroclasts, which indicate crystallization of olivine at the expenses of orthopyroxene, and (3) the olivine-orthopyroxene mixing in the pressure shadows of the orthopyroxene porphyroclasts, which indicates re-precipitation of orthopyroxene at mm distances. Further fluid focusing, leading to an increase in the contribution of dissolution-precipitation creep to the deformation, is corroborated by the enrichment in amphibole and by the analysis of the olivine-orthopyroxene shapes, spatial arrangements, and CPO in the Ultramylonite bands. Changes in Si molality of the percolating fluid allowed for alternating dissolution and precipitation of Si (crystallization of olivine at the expenses of orthopyroxene and vice versa), accounting for redistribution of both minerals in the ultramylonites. The increasing contribution of dissolution-precipitation to deformation is also recorded by the marked decrease in the strength of olivine CPO from the Mylonite to Ultramylonite-1 bands and the almost random olivine CPO in the Ultramylonite-2 bands. It is also supported by the atypical orthopyroxene CPO in the shear zone, which cannot be explained by dislocation creep and probably results from synkinematic oriented crystallization and growth.

The present study demonstrates that dissolution-precipitation creep may be an effective deformation process in the shallow upper mantle at temperature conditions *ca.* 750-1000 °C. It

ACCEPTED MANUSCRIPT

also points to strong feedbacks between deformation and permeability, leading to fluid focusing in actively deforming strain zones. In the studied shear zone, extensive dissolution-precipitation is restricted to mm-scale ultramylonite zones due to limited fluid availability. However, dissolution-precipitation creep might play an important role in the deformation of some domains of the mantle wedge above subduction zones, where large amounts of fluids may be present. In this case, we may, based on the present data, envisage major feedback between deformation and fluid transport.

Acknowledgements

We thank C. Nevado, D. Delmas (GM, France), and R. Reyes-González (IACT, Spain) for sample preparation and thin section polishing, and B. Boyer and C. Merlet (GM, France) for assistance with EPMA analyses. We acknowledge the constructive criticism and helpful comments of the two reviewers, K. Michibayashi and L. F. G. Morales, and the Lithos Editor, M. Scambelluri.

Research leading to these results was funded by the European Union Framework Programme 7 (EU-FP7) Marie Curie postdoctoral grant PIEF-GA-2012-327226 to K.H. C.M.'s work was funded by a MINECO Ramón y Cajal Fellowship (RYC-2012-11314). C.J.G. acknowledges grants from the International Lithosphere Program (CC4-MEDYNA), the Spanish Ministry of Economy and Competitiveness (MINECO) (CGL2013-42349-P and PCIN-2015-053), and the Junta de Andalucía (RNM-131). This research have been funded partly by EU Cohesion Policy funds from the European Regional Development Fund and the European Social Fund in support of human resources, innovation, increasing research capacities, and research infrastructures.

ACCEPTED MANUSCRIPT

References

Austrheim, H., 1987. Eclogitization of lower crustal granulites by fluid migration through shear zones. Earth and Planetary Science Letters 81, 221-232.

Bachmann, F., Hielscher, R., Schaeben, H., 2010. Texture analysis with MTEX - free and open source software toolbox. Solid State Phenomena 160, 63-68.

Bali, E., Bolfan-Casanova, N., Koga, K.T., 2008. Pressure and temperature dependence of H solubility in forsterite: An implication to water activity in the Earth interior. Earth and Planetary Science Letters 268, 354-363.

Bestmann, M., Prior, D.J., Veltkamp, K.T.A., 2004. Development of single-crystal σ-shaped quartz porphyroclasts by dissolution–precipitation creep in a calcite marble shear zone. Journal of Structural Geology 26, 869-883.

Brey, G.P., Köhler, T.P., 1990. Geothermobarometry in four phase lherzolites II. New thermobarometers and practical assessment of existing thermobarometers. Journal of Petrology 31, 1353-1378.

Bunge, H.J., 1982. Texture analysis in materials sciences. Buttleworth, London.

Carter, N., Avé Lallemant, H., 1970. High temperature flow of dunite and peridotite. Bulletin of the Geological Society of America 81, 2181-2202.

Cassard, D., 1980. Structure et origine des gisements de chromite du Massif du Sud-Ophiolites de Nouvelle-Caldonie. Ph.D. thesis, Univ. Nantes.

Cherniak, D.J., Dimanov, A., 2010. Diffusion in Pyroxene, Mica and Amphibole. Reviews in Mineralogy and Geochemistry 72, 641-690.

ACCEPTED MANUSCRIPT

Chokshi, A.H., Langdon, T.G., 1987. A model for diffusional cavity growth in superplasticity. Acta Metallurgica 35, 1089-1101.

Connolly, J.A.D., 2009. The geodynamic equation of state: What and how. Geochemistry Geophysics Geosystems 10.

Costa, F., Chakraborty, S., 2008. The effect of water on Si and O diffusion rates in olivine and implications for transport properties and processes in the upper mantle. Physics of the Earth and Planetary Interiors 166, 11-29.

Czertowicz, T.A., Toy, V.G., Scott, J.M., 2016. Recrystallization, phase mixing and strain localisation in peridotite during rapid extrusion of sub-arc mantle lithosphere. Journal of Structural Geology 88, 1-19.

Dabrowski, M., Schmid, D.W., Podladchikov, Y.Y., 2012. A two-phase composite in simple shear: Effective mechanical anisotropy development and localization potential. Journal of Geophysical Research: Solid Earth 117

Demouchy, S., Tommasi, A., Barou, F., Mainprice, D., Cordier, P., 2012. Deformation of olivine in torsion under hydrous conditions. Physics of the Earth and Planetary Interiors 202, 56-70.

Demouchy, S., Tommasi, A., Ballaran, T.B., Cordier, P., 2013. Low strength of Earth's uppermost mantle inferred from tri-axial deformation experiments on dry olivine crystals. Physics of the Earth and Planetary Interiors 220, 37-49.

Demouchy, S., Mussi, A., Barou, F., Tommasi, A., Cordier, P., 2014. Viscoplasticity of polycrystalline olivine experimentally deformed at high pressure and 900 °C. Tectonophysics 623, 123-135.

ACCEPTED MANUSCRIPT

Dijkstra, A.H., Drury, M.R., Vissers, R.L.M., Newman, J., 2002. On the role of melt-rock reaction in mantle shear zone formation in the Othris Peridotite Massif (Greece). Journal of Structural Geology 24, 1431-1450.

Di Leo, J.F., Wookey, J., Hammond, J.O.S., Kendall, J.M., Kaneshima, S., Inoue, H., Yamashina, T., Harjadi, P., 2012. Deformation and mantle flow beneath the Sangihe subduction zone from seismic anisotropy. Physics of the Earth and Planetary Interiors 194–195, 38-54.

Durham, W.B., Goetze, C., 1977. Plastic flow of oriented single crytals of olivine: 1 – mechanical data. J. Geophys. Res. 82, 5737–5753.

Fei, H., Hegoda, C., Yamazaki, D., Wiedenbeck, M., Yurimoto, H., Shcheka, S., Katsura, T., 2012. High silicon self-diffusion coefficient in dry forsterite. Earth and Planetary Science Letters 345–348, 95-103.

Fei, H., Wiedenbeck, M., Yamazaki, D., Katsura, T., 2013. Small effect of water on upper-mantle rheology based on silicon self-diffusion coefficients. Nature 498, 213-215.

Fei, H., Wiedenbeck, M., Yamazaki, D., Katsura, T., 2014. No effect of water on oxygen self-diffusion rate in forsterite. Journal of Geophysical Research: Solid Earth, 2014JB011141.

Frets, E.C., Tommasi, A., Garrido, C.J., Vauchez, A., Mainprice, D., Targuisti, K., Amri, I., 2014. The Beni Bousera Peridotite (Rif Belt, Morocco): an Oblique-slip Low-angle Shear Zone Thinning the Subcontinental Mantle Lithosphere. Journal of Petrology 55, 283-313.

Furusho, M., Kanagawa, K., 1999. Transformation induced strain localization in a lherzolite mylonite from the Hidaka metamorphic belt of central Hokkaido, Japan. Tectonophysics 313, 411-432.

ACCEPTED MANUSCRIPT

Garrido, C.J., Gueydan, F., Booth-Rea, G., Precigout, J., Hidas, K., Padrón-Navarta, J.A., Marchesi, C., 2011. Garnet lherzolite and garnet-spinel mylonite in the Ronda peridotite: Vestiges of Oligocene backarc mantle lithospheric extension in the western Mediterranean. Geology 39, 927-930.

Girard, J., Chen, J., Raterron, P., & Holyoke, C. W., 2013. Hydrolytic weakening of olivine at mantle pressure: Evidence of [100](010) slip system softening from single-crystal deformation experiments. Phys. Earth Planet. Inter. 216, 12-20.

Green, D.H., 1973. Experimental melting studies on a model upper mantle composition at high pressure under water-saturated and water-undersaturated conditions. Earth and Planetary Science Letters 19, 37-53.

Green, D. H., Hibberson, W. O., Kovács, I., Rosenthal, A., 2010. Water and its influence on the lithosphere-asthenosphere boundary. Nature 467, 448-U497.

Hidas, K., Booth-Rea, G., Garrido, C.J., Martinez-Martinez, J.M., Padrón-Navarta, J.A., Konc, Z., Giaconia, F., Frets, E., Marchesi, C., 2013a. Backarc basin inversion and subcontinental mantle emplacement in the crust: kilometre-scale folding and shearing at the base of the proto-Alborán lithospheric mantle (Betic Cordillera, southern Spain). Journal of the Geological Society, London 170, 47-55.

Hidas, K., Garrido, C.J., Tommasi, A., Padrón-Navarta, J.A., Thielmann, M., Konc, Z., Frets, E., Marchesi, C., 2013b. Strain localization in pyroxenite by reaction-enhanced softening in the shallow subcontinental lithospheric mantle. Journal of Petrology 54, 1997-2031.

Hidas, K., Varas-Reus, M.I., Garrido, C.J., Marchesi, C., Acosta-Vigil, A., Padrón-Navarta, J.A., Targuisti, K., Konc, Z., 2015. Hyperextension of continental to oceanic-like lithosphere: The

ACCEPTED MANUSCRIPT

record of late gabbros in the shallow subcontinental lithospheric mantle of the westernmost Mediterranean. Tectonophysics 650, 65-79.

Hiraga, T., Miyazaki, T., Yoshida, H., Zimmerman, M.E., 2013. Comparison of microstructures in superplastically deformed synthetic materials and natural mylonites: Mineral aggregation via grain boundary sliding. Geology 41, 959-962.

Holland, T.J.B., Powell, R., 1998. An internally consistent thermodynamic data set for phases of petrological interest. Journal of Metamorphic Geology 16, 309-343.

Holtzman, B.K., 2016. Questions on the existence, persistence and mechanical effects of a very small melt fraction in the asthenosphere. Geochemistry, Geophysics, Geosystems 17, 470-484.

Jung, H., Park, M., Jung, S., Lee, J., 2010. Lattice preferred orientation, water content, and seismic anisotropy of orthopyroxene. J. Earth Sci. 21, 555-568.

Kaczmarek, M.-A., Tommasi, A., 2011. Anatomy of an extensional shear zone in the mantle, Lanzo massif, Italy. Geochem. Geophys. Geosyst. 12, Q0AG06.

Karato, S.-I. (2008). Deformation of Earth Materials: An introduction to the rheology of solid Earth. Cambridge University Press, Cambridge, New York, pp. 463.

Karato, S.-I., Toriumi, M., Fujii, T., 1980. Dynamic recrystallization of olivine single crystals during high-temperature creep. Geophysical Research Letters 7, 649-652.

Katayama, I., Jung, H., Karato, S.I., 2004. New type of olivine fabric from deformation experiments at modest water content and low stress. Geology 32, 1045-1048.

Linckens, J., Bruijn, R.H.C., Skemer, P., 2014. Dynamic recrystallization and phase mixing in experimentally deformed peridotite. Earth and Planetary Science Letters 388, 134-142.

ACCEPTED MANUSCRIPT

Long, M.D., Silver, P.G., 2008. The Subduction Zone Flow Field from Seismic Anisotropy: A Global View. Science 319, 315-318.

Mainprice, D., Tommasi, A., Couvy, H., Cordier, P., Frost, D.J., 2005. Pressure sensitivity of olivine slip systems and seismic anisotropy of Earth's upper mantle. Nature 433, 731-733.

Mainprice, D., Bachmann, F., Hielscher, R., Schaeben, H., 2014. Descriptive tools for the analysis of texture projects with large datasets using MTEX: strength, symmetry and components. Geological Society, London, Special Publications 409.

Manning, C. E., 1994. The solubility of quartz in H_2O in the lower crust and upper mantle. Geochimica et Cosmochimica Acta 58, 4831-4839.

Manning, C. E., Antignano, A., Lin, H. A., 2010. Premelting polymerization of crustal and mantle fluids, as indicated by the solubility of albite + paragonite + quartz in H_2O at 1 GPa and 350–620 °C. Earth and Planetary Science Letters 292, 325-336.

Marchesi, C., Garrido, C.J., Bosch, D., Bodinier, J.-L., Hidas, K., Padrón-Navarta, J.A., Gervilla, F., 2012. A late Oligocene suprasubduction setting in the westernmost Mediterranean revealed by intrusive pyroxenite dikes in the Ronda Peridotite (southern Spain). The Journal of Geology 120, 237-247.

McInnes, B. I., Gregoire, M., Binns, R. A., Herzig, P. M., & Hannington, M. D., 2001. Hydrous metasomatism of oceanic sub-arc mantle, Lihir, Papua New Guinea: petrology and geochemistry of fluid-metasomatised mantle wedge xenoliths. Earth Planet. Sci. Lett. 188, 169-183.

Mehl, L., Hacker, B.R., Hirth, G., Kelemen, P.B., 2003. Arc-parallel flow within the mantle wedge: Evidence from the accreted Talkeetna arc, south central Alaska. Journal of Geophysical Research: Solid Earth 108, B8, 2375.

ACCEPTED MANUSCRIPT

Mei, S., Kohlstedt, D.L., 2000a. Influence of water on plastic deformation of olivine aggregates: 1. Diffusion creep regime. Journal of Geophysical Research: Solid Earth 105, 21457-21469.

Mei, S., Kohlstedt, D.L., 2000b. Influence of water on plastic deformation of olivine aggregates: 2. Dislocation creep regime. Journal of Geophysical Research: Solid Earth 105, 21471-21481.

Menegon, L., Pennacchioni, G., Spiess, R. (2008). Dissolution-precipitation creep of K-feldspar in mid-crustal granite mylonites. Journal of Structural Geology 30, 565-579.

Michibayashi, K., Mainprice, D., 2004. The role of pre-existing mechanical anisotropy on shear zone development within oceanic mantle lithosphere: an example from the Oman Ophiolite. Journal of Petrology 45, 405-414.

Michibayashi, K., Oohara, T., 2013. Olivine fabric evolution in a hydrated ductile shear zone at the Moho Transition Zone, Oman Ophiolite. Earth and Planetary Science Letters 377–378, 299-310.

Milke, R., Dohmen, R., Becker, H. W., Wirth, R., 2007. Growth kinetics of enstatite reaction rims studied on nano-scale, Part I: Methodology, microscopic observations and the role of water. Contributions to Mineralogy and Petrology 154, 519-533.

Milke, R., Kolzer, K., Koch-Müller, M., Wunder, B., 2009. Orthopyroxene rim growth between olivine and quartz at low temperatures (750–950 °C) and low water concentration. Mineralogy and Petrology 97, 223-232.

Milke, R., Abart, R., Keller, L., Rhede, D., 2011. The behavior of Mg, Fe, and Ni during the replacement of olivine by orthopyroxene: Experiments relevant to mantle metasomatism: Mineralogy and Petrology 103, 1–8.

Milke, R., Neusser, G., Kolzer, K., Wunder, B., 2013. Very little water is necessary to make a dry solid silicate system wet. Geology 41, 247-250.

Miyazaki, T., Sueyoshi, K., & Hiraga, T., 2013. Olivine crystals align during diffusion creep of Earth's upper mantle. Nature 502, 321-326.

ACCEPTED MANUSCRIPT

Naze, L., Doukhan, N., Doukhan, J.C., Latrous, K., 1987. A TEM study of lattice-defects in naturally and experimentally deformed orthopyroxenes. Bulletin De Mineralogie 110, 497-512.

Newman, J., Lamb, W.M., Drury, M.R., Vissers, R.L.M., 1999. Deformation processes in a peridotite shear zone: reaction-softening by an H_2O-deficient, continuous net transfer reaction. Tectonophysics 303, 193-222.

Newton, R.C., Manning, C.E., 2002. Solubility of enstatite + forsterite in H_2O at deep crust/upper mantle conditions: 4 to 15 kbar and 700 to 900 °C. Geochimica et Cosmochimica Acta 66, 4165-4176.

Padrón-Navarta, J. A., Tommasi, A., Garrido, C. J., López Sánchez-Vizcaíno, V., Gómez-Pugnaire, M. T., Jabaloy, A., Vauchez, A. (2010a). Fluid transfer into the wedge controlled by high-pressure hydrofracturing in the cold top-slab mantle. Earth and Planetary Science Letters 297, 271-286.

Padrón-Navarta, J.A., Hermann, J., Garrido, C.J., López Sánchez-Vizcaíno, V., Gómez-Pugnaire, M.T., 2010b. An experimental investigation of antigorite dehydration in natural silica-enriched serpentinite. Contributions to Mineralogy and Petrology 159, 25-42.

Petry, C., Chakraborty, S., Palme, H., 2004. Experimental determination of Ni diffusion coefficients in olivine and their dependence on temperature, composition, oxygen fugacity, and crystallographic orientation. Geochimica et Cosmochimica Acta 68, 4179-4188.

Precigout, J., Gueydan, F., Garrido, C.J., Cogne, N., Booth-Rea, G., 2013. Deformation and exhumation of the Ronda peridotite (Spain). Tectonics 32, 1011-1025.

Putnis, A., 2015. Transient Porosity Resulting from Fluid–Mineral Interaction and its Consequences. Reviews in Mineralogy and Geochemistry 80, 1-23.

ACCEPTED MANUSCRIPT

Ree, J.H., 1994. Grain-boundary sliding and development of grain-boundary openings in experimentally deformed octachloropropane. Journal of Structural Geology 16, 403-418.

Rutter, E.H., 1976. The kinetics of rocks deformation by pressure solution. Philos. Trans. R. Soc. Lond. A283, 203-219.

Soustelle, V., Tommasi, A., Bodinier, J.-L., Garrido, C. J., Vauchez, A., 2009. Deformation and reactive melt transport in the mantle lithosphere above a large-scale partial melting domain: the Ronda Peridotite Massif, southern Spain. Journal of Petrology 50, 1235-1266.

Soustelle, V., Tommasi, A., Demouchy, S., Ionov, D.A., 2010. Deformation and Fluid–Rock Interaction in the Supra-subduction Mantle: Microstructures and Water Contents in Peridotite Xenoliths from the Avacha Volcano, Kamchatka. Journal of Petrology 51, 363-394.

Spiers, C.J., De Meer, S., Niemeijer, A.R., Zhang, X., 2004. Kinetics of rock deformation by pressure solution and the role of thin aqueous films, in: Nakashima, S., Spiers, C.J., Mercury, L., Fenter, P.A., Hocheller, M.F. (Eds.), Physicochemistry of Water in Geological and Biological Systems: Structures and Properties of Thin Aqueous Films. Universal Academy Press, Inc., Tokyo, pp. 129-158.

Steuten, J. M., & Van Roermund, H. L. M., 1989. An optical and electron microscopy study of defect structures in naturally deformed orthopyroxene. Tectonophysics 157, 331-338.

Stöckhert, B., Wachmann, M., Küster, M., Bimmermann, S. (1999). Low effective viscosity during high pressure metamorphism due to dissolution precipitation creep: the record of HP–LT metamorphic carbonates and siliciclastic rocks from Crete. Tectonophysics 303, 299-319.

Suhr, G., 1993. Evaluation of upper mantle microstructures in the Table Mountain massif (Bay of Islands ophiolite). Journal of Structural Geology 15, 1273-1292.

ACCEPTED MANUSCRIPT

Sundberg, M., Cooper, R.F., 2008. Crystallographic preferred orientation produced by diffusional creep of harzburgite: Effects of chemical interactions among phases during plastic flow. Journal of Geophysical Research-Solid Earth 113.

Takei, Y., 1998. Constitutive mechanical relations of solid-liquid composites in terms of grain-boundary contiguity, J. Geophys. Res. 103, 18183–18203.

Tarantola, A., Valette, B., 1982. Generalized nonlinear inverse problems solved using the least squares criterion. Reviews of Geophysics 20, 219-232.

Tommasi, A., Vauchez, A. 2015. Heterogeneity and anisotropy in the lithospheric mantle. Tectonophysics 661, 11-37.

Tommasi, A., Vauchez, A., Godard, M., Belley, F., 2006. Deformation and melt transport in a highly depleted peridotite massif from the Canadian Cordillera: Implications to seismic anisotropy above subduction zones. Earth and Planetary Science Letters 252, 245-259.

Tullis, J., Yund, R., Farver, J. (1996). Deformation-enhanced fluid distribution in feldspar aggregates and implications for ductile shear zones. Geology 24, 63-66.

Urai, J.L., Spiers, C.J., Zwart, H.J., Lister, G.S., 1986. Weakening of rock salt by water during long-term creep. Nature 324, 554-557.

Van der Wal, D., Chopra, P., Drury, M., Gerald, J.F., 1993. Relationships between dynamically recrystallized grain size and deformation conditions in experimentally deformed olivine rocks. Geophysical Research Letters 20, 1479-1482.

Van der Wal, D., Vissers, R.L.M., 1996. Structural petrology of the Ronda peridotite, SW Spain: Deformation history. Journal of Petrology 37, 23-43.

ACCEPTED MANUSCRIPT

Van Keken, P.E., Kiefer, B., Peacock, S.M., 2002. High-resolution models of subduction zones: Implications for mineral dehydration reactions and the transport of water into the deep mantle. Geochemistry Geophysics Geosystems 3.

Vauchez, A., Tommasi, A., Mainprice, D., 2012. Faults (shear zones) in the Earth's mantle. Tectonophysics 558, 1-27.

Vissers, R.L.M., Drury, M.R., Strating, E.H.H., Spiers, C.J., Vanderwal, D., 1995. Mantle shear zones and their effect on lithosphere strength during continental breakup. Tectonophysics 249, 155-171.

Warren, J.M., Hirth, G., 2006. Grain size sensitive deformation mechanisms in naturally deformed peridotites. Earth and Planetary Science Letters 248, 438-450.

Wassmann, S., Stöckhert, B., 2013. Rheology of the plate interface — Dissolution precipitation creep in high pressure metamorphic rocks. Tectonophysics 608, 1-29.

Webber, C. E., Little, T., Newman, J., & Tikoff, B., 2008. Fabric superposition in upper mantle peridotite, Red Hills, New Zealand. J. Struct. Geol. 30, 1412-1428.

Wheeler, J., 1987. The significance of grain-scale stresses in the kinetics of metamorphism. Contributions to Mineralogy and Petrology 97, 397-404.

Wheeler, J., 2009. The preservation of seismic anisotropy in the Earth's mantle during diffusion creep. Geophysical Journal International 178, 1723-1732.

Wintsch, R.P., Yi, K., 2002. Dissolution and replacement creep: a significant deformation mechanism in mid-crustal rocks. Journal of Structural Geology 24, 1179-1193.

Witt-Eickschen, G., Seck, H.A., 1991. Solubility of Ca and Al in orthopyroxene from spinel peridotite - an improved version of an empirical geothermometer. Contributions to Mineralogy and Petrology 106, 431-439.

ACCEPTED MANUSCRIPT

Zhang, Y.-G., Frantz, J.D., 2000. Enstatite-forsterite-water equilibria at elevated temperatures and pressures. American Mineralogist 85, 918-925

ACCEPTED MANUSCRIPT

Figure captions

Figure 1: Structures in the study area and sampling sites. Inset shows the tectono-metamorphic domains of the Ronda Peridotite (see Hidas et al., 2013a for references) and the location of the study area. From NNW to SSE, the Ronda Peridotite massif is composed of: [1] garnet-spinel mylonites; [2] spinel tectonites; [3] the recrystallization front; [4] granular spinel peridotites; [5] plagioclase tectonites. The Blanca crustal unit has a tectonic contact with the massif. In the study area, we observe a pyroxenite layering, which is crosscut by a pervasive high-temperature foliation, visible only in plagioclase-peridotites (red symbols), and lower-temperature foliations defined by a marked grain size reduction (blue symbols) in mylonitic and ultramylonitic peridotite or pyroxenite shear zones that crosscut all lithologies.

Figure 2: Outcrops of the widest segment (a) and the tip (b) of the shear zone characterized by alternating olivine-rich Mylonite lenses (darker) and orthopyroxene-rich Ultramylonite (brighter) bands. White-shaded planes indicate the strike and dip of shear zone foliation (*cf.* Fig. 1). Labels – Ol: olivine; Opx: orthopyroxene; Spl: spinel.

Figure 3: EBSD phase-map (a) and cross-polarized light photomicrographs (b-c) of the coarse-grained protolith of the shear zone (sample RK025). Insets show the location of corresponding figures. Labels – Ol: olivine; Opx: orthopyroxene; Cpx: clinopyroxene; Spl: spinel.

Figure 4: Modal compositions calculated from whole rock XRF (in anhydrous wt.%) and mineral chemistry data for representative samples of the host peridotite and the shear zone (Table

ACCEPTED MANUSCRIPT

1) and variations in modal composition among the different microstructural domains of the shear zone determined from EBSD phase maps (in area%).

Figure 5: Cross-polarized light photomicrograph (a) and EBSD phase-maps (b-e) showing the microstructures within the shear zone. (a) Mylonite and Ultramylonite-1 from the widest segment of the shear zone in sample RK042. Note the relict olivine porphyroclasts in the Mylonite (one, which is almost fully recrystallized, is outlined with white dashed line) and the highly stretched orthopyroxene porphyroclasts. (b) Composite view of the thin section with EBSD phase map on the left and plane polarized-light photomicrograph on the right showing Mylonite lenses surrounded by Ultramylonite-1 bands and crosscut by more planar Ultramylonite-2 bands in sample RK167, collected close to the tip of the shear zone. (c) EBSD phase map for sample RK109, collected at the intermediate section of the shear zone, showing Mylonite lenses surrounded by Ultramylonite-1 bands. The irregular limits between the two microstructural domains are underlined in white. White dashed line in the Mylonite lens indicate an elongated olivine porphyroclast and white arrows point at embayments of orthopyroxene porphyroclast filled by olivine. Note (1) the corroded grain boundaries of orthopyroxene porphyroclasts and their tails composed by fine-grained, well-mixed olivine-orthopyroxene assemblages that grade into Ultramylonite-1 bands, (2) the interstitial fine-grained orthopyroxene crystals at the edges of olivine-rich Mylonite lenses, and (3) the subgrain boundaries perpendicular to the grain elongation in the inset. (d) Detail of an Ultramylonite-1 band in sample RK167; note the enrichment in clinopyroxene and amphibole. (e) Detail of an Ultramylonite-2 band in sample RK167. Insets in (d-e) show elongated, small orthopyroxenes precipitated on the olivine crystal faces under compression in both Ultramylonite bands. Note

ACCEPTED MANUSCRIPT

that olivine and orthopyroxene have irregular shapes and highly indented grain boundaries in both types of ultramylonites. See composite view (b) for location of (d) and (e) in the thin section. Labels – Amp: amphibole; Cpx: clinopyroxene; Ol: olivine; Opx: orthopyroxene; Spl: spinel; UMYL-2: Ultramylonite-2.

Figure 6: Shape factor (a-c) and aspect ratio (d-f) as a function of equivalent diameter (in µm) of olivine (red) and orthopyroxene (blue) in the (a,d) Mylonite lenses, (b,e) Ultramylonite-1, and (c,f) Ultramylonite-2 bands in various shear zone samples. The diagrams for Mylonite also include the grain analyses of the porphyroclasts (vertical dashed lines denote the empirical threshold used to distinguish porphyroclasts from the neoblasts), hence the logarithmic scale in (a) and (d). Scaling for Ultramylonites is linear. The gray shaded areas underline the 0-70 µm grain diameter domain in all diagrams. The white circles and triangles indicate the area-weighted mean grain size of olivine and orthopyroxene, respectively. In (a,d) error bars indicate the variability of the data between different samples within a microstructural domain. The equivalent diameter of a grain is the diameter of a circle that has the same area as the grain. The shape factor is the ratio between the perimeter of a grain and the perimeter of an equal-area circle. The area-weighted mean grain size of olivine or orthopyroxene is used to avoid overrepresentation of the smallest grain fraction, which contains a large number of grains, but occupies a limited surface in the sample.

Figure 7: Pole figures showing the Crystal Preferred Orientation (CPO) of olivine and orthopyroxene and inverse pole figures in the crystal reference frame displaying the rotation axes accommodating low-angle (2-15°) misorientations in the coarse-grained protolith and in the

ACCEPTED MANUSCRIPT

different microstructural domains of the shear zone. Pole figures are lower hemisphere, equal-area stereographic projections; contours as 0.5 multiples of a uniform distribution, black square: maximum density. Pole figures are plotted using the average orientation of each grain ('one point per grain') to avoid over-representation of large porphyroclasts in the thin sections. All data are presented in the structural reference frame of the shear zone; the full line denotes the average orientation of the foliation and lineation is indicated by a white star. For the protolith, the dashed line indicates the average orientation of the foliation in the shear zone and the dotted one represents the average orientation of the high-T foliation in nearby plagioclase tectonites (Fig. 1). Labels – n: number of measured grains; J_{Ol} and J_{Opx} are the J-indices of olivine and orthopyroxene, respectively; UMYL-2: Ultramylonite-2.

Figure 8: Calculated temperatures using the Ca-in-Opx method of Brey and Köhler (1990) and the Cr-Al-Opx method of Witt-Eickschen and Seck (1991) based on orthopyroxene major element chemical data. The effect of pressure on temperature estimates using the Ca-in-Opx method is depicted by presenting the values estimated for 0.8 GPa by symbols and those for a pressure range of 0.5-1.5 GPa by vertical bars. The 0.8 GPa value corresponds to the pressure of spinel to plagioclase phase transformation reaction responsible for development of small-scale shear zones in nearby pyroxenites with a kinematics similar to the presently studied shear zone (Hidas et al., 2013a,b). For comparison, we show pre- and post-kinematic conditions reconstructed by Perple_X thermodynamic modeling for these pyroxenites (Hidas et al., 2013b). Tlc-in, Chl-in and Amp-out indicate the temperature ranges for the appearance of talc and chlorite, and disappearance of amphibole at 0.8 GPa, respectively, calculated using Perple_X (Fig. 9).

ACCEPTED MANUSCRIPT

Figure 9: Computed isochemical section for the protolith (RK026; Table 1) with calculated modal amount of amphibole (colored lines; values in vol%) for water-saturated conditions. Subsolidus phase relations have been computed in the CrNFCMASH (Cr_2O_3-Na_2O-FeO-CaO-MgO-Al_2O_3-SiO_2-H_2O) system with Perple_X (Connolly, 2009), and the updated internally consistent thermodynamic dataset of Holland and Powell (1998, updated in 2002) extended to include Cr-bearing phases (cr_hp02ver.dat). Gray shading represents the variance (*i.e.* number of phases) within the field, darker shades indicate fewer stable phases. Yellow-shaded domain bordered by dotted yellow line shows the most likely final re-equilibration PT conditions for the protolith and the shear zone. Temperature limits of the box are estimated based on petrography (lack of chlorite and plagioclase) and geothermometric calculations. Maximum pressure of equilibration in the shear zone during deformation around 0.8 GPa is constrained by the spinel to plagioclase phase transformation reaction in the nearby pyroxenite shear zone (Hidas et al., 2013b). Labels – Amp*: tremolite and pargasite; Atg: antigorite; Chl: chlorite; Cpx: clinopyroxene; Ol: olivine; Parg: pargasite; Plag: plagioclase; Spl: spinel; Tlc: talc; Tr: tremolite.

ACCEPTED MANUSCRIPT

Table captions

Table 1: Modal compositions and whole rock major element concentrations (in wt%) in the coarse-grained protolith and the shear zone. Mineral modes of the protolith and shear zone whole rocks (WR) have been reconstructed by averaging the mass-balance of whole rock and mineral major element compositions, using the total inversion method of Tarantola and Valette (1982); modal proportions in anhydrous weight percent, marked by a star. Due to the lack of any characteristic major element, the amount of amphibole cannot be estimated with this method. Mineral modes of amphibole in the whole rocks (both the protolith and the shear zone) and those of the other constituent phases in the microstructural domains of the shear zone are calculated by averaging out EBSD phase maps weighted by the area of the maps; modal proportions in area percent. To calculate the whole rock modal composition of the shear zone with this method, we assumed a Mylonite:Ultramylonite-1 ratio of 30:70 (*cf.* Fig. 2). Numbers in parentheses at the Mylonite represent values if the orthopyroxene porphyroclasts are not included in this domain. Labels – Amp: amphibole; Cpx: clinopyroxene; Ol: olivine; Opx: orthopyroxene; Spl: spinel. For whole rock major and minor transition element (*e.g.*, Ni, Cr) analyses, samples were crushed and pulverized in a Pulverisette agate mortar. FeO_t: all iron reported as Fe^{2+}; LOI: loss on ignition; mg#=[Mg/(Mg+Fe)] in cation ratio. Note that samples names are reported only to identify analyses and do not correspond to microstructural domains in the upper part of the table, which are averages of various analyses.

ACCEPTED MANUSCRIPT

Supplementary Table S1: Electron microprobe analyses (EPMA) of minerals (in wt %). FeO*: all iron reported as Fe^{2+}; Cr#=Cr/(Cr+Al) and Mg#=Mg/(Mg+Fe) expressed in cation numbers of atomic per formula units; nd: not detected.

ACCEPTED MANUSCRIPT

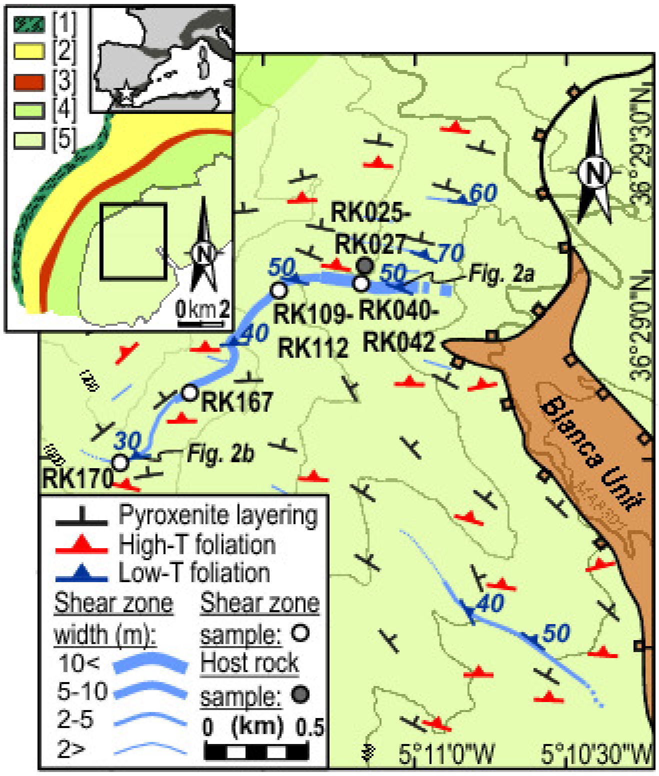

Fig. 1 Hidas et al.

ACCEPTED MANUSCRIPT

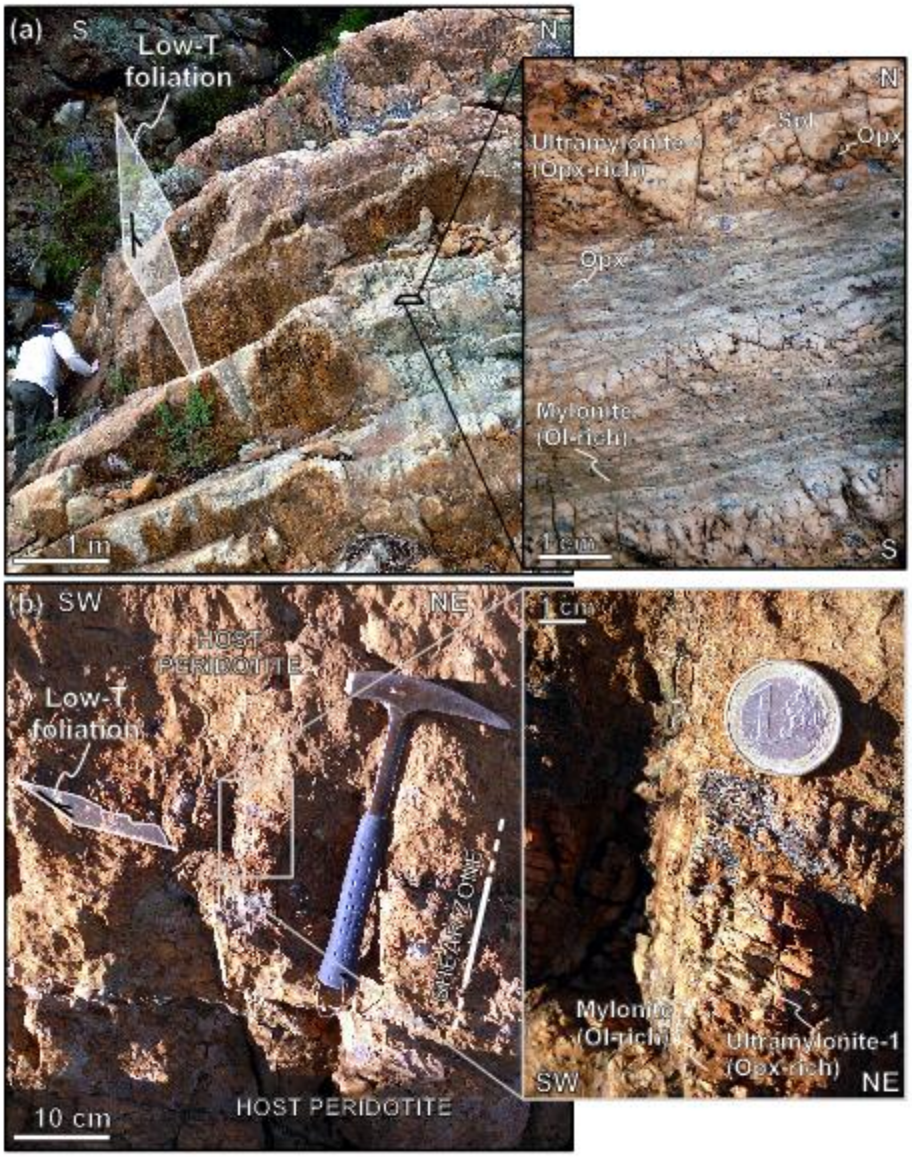

Fig. 2 Hidas et al.

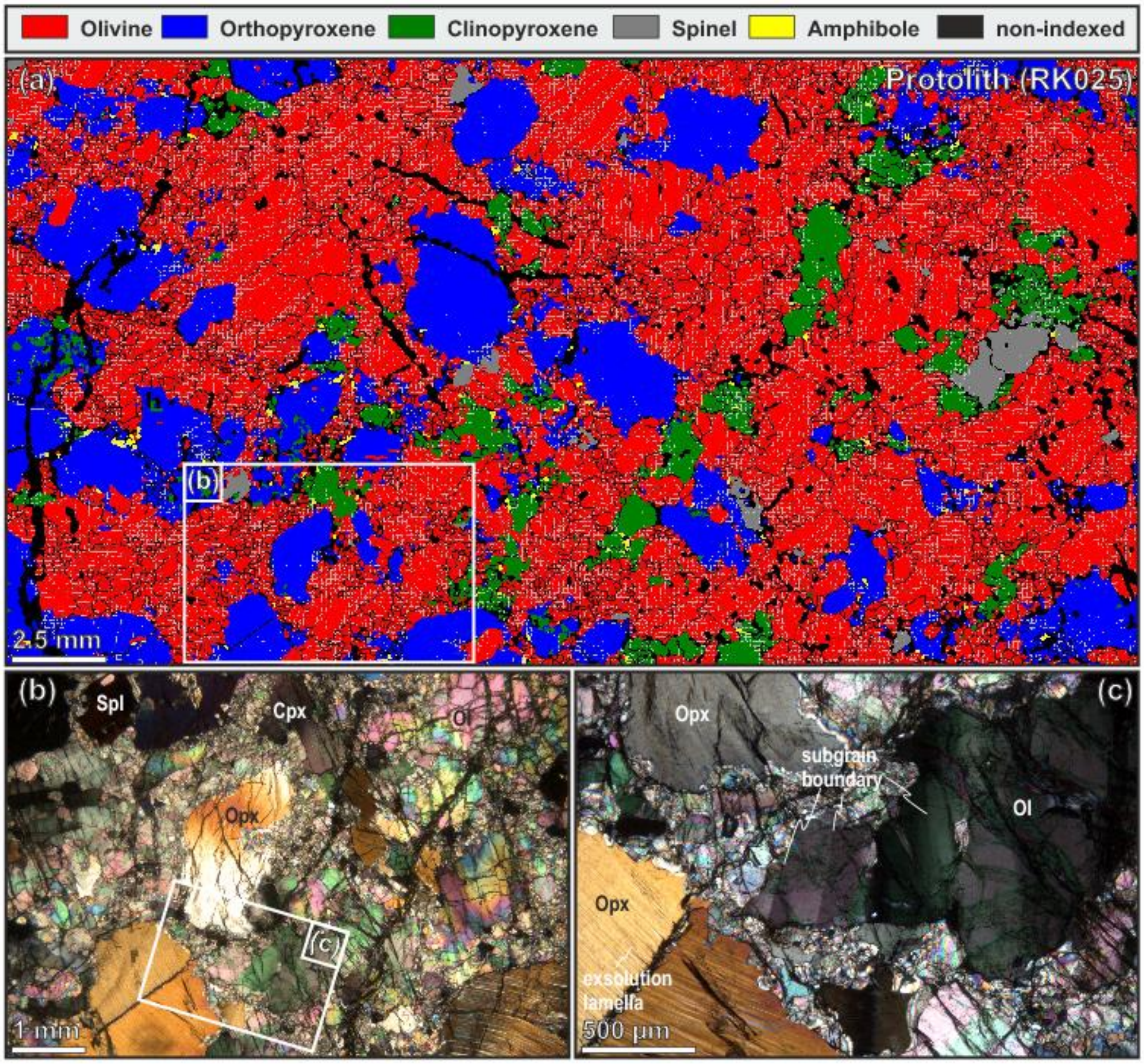

Fig. 3 Hidas et al.

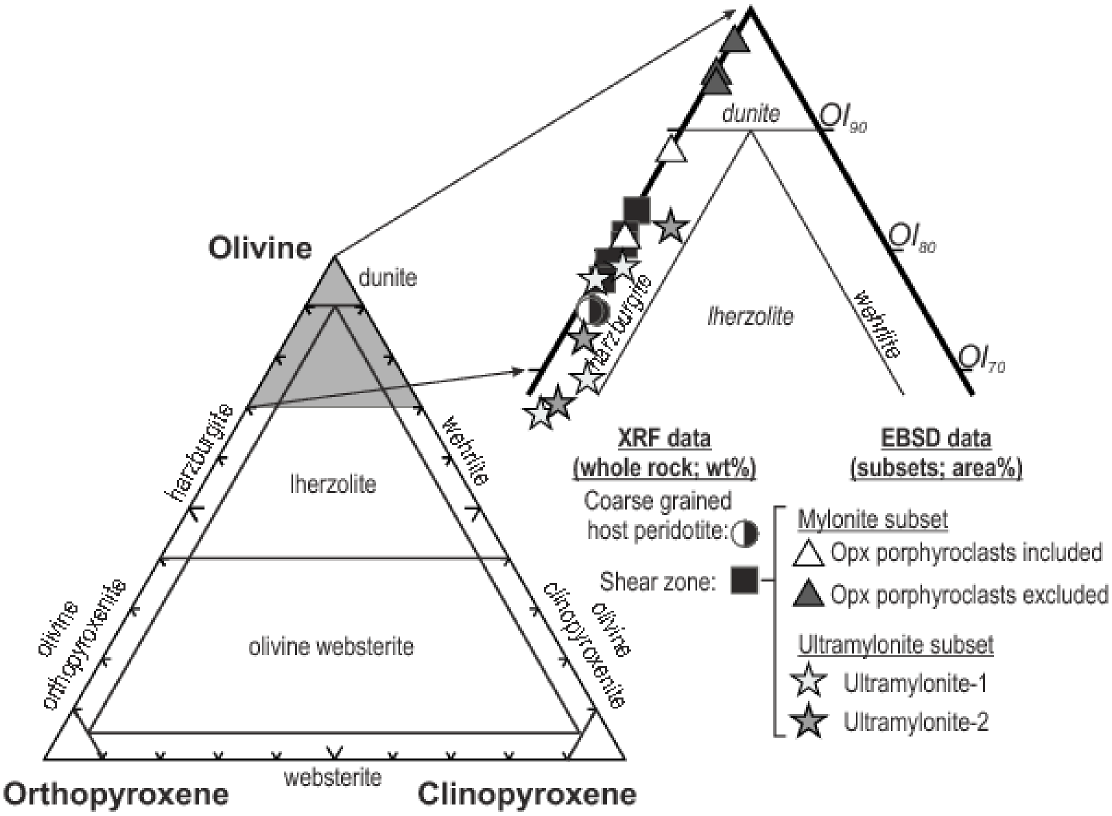

Fig. 4 Hidas et al.

ACCEPTED MANUSCRIPT

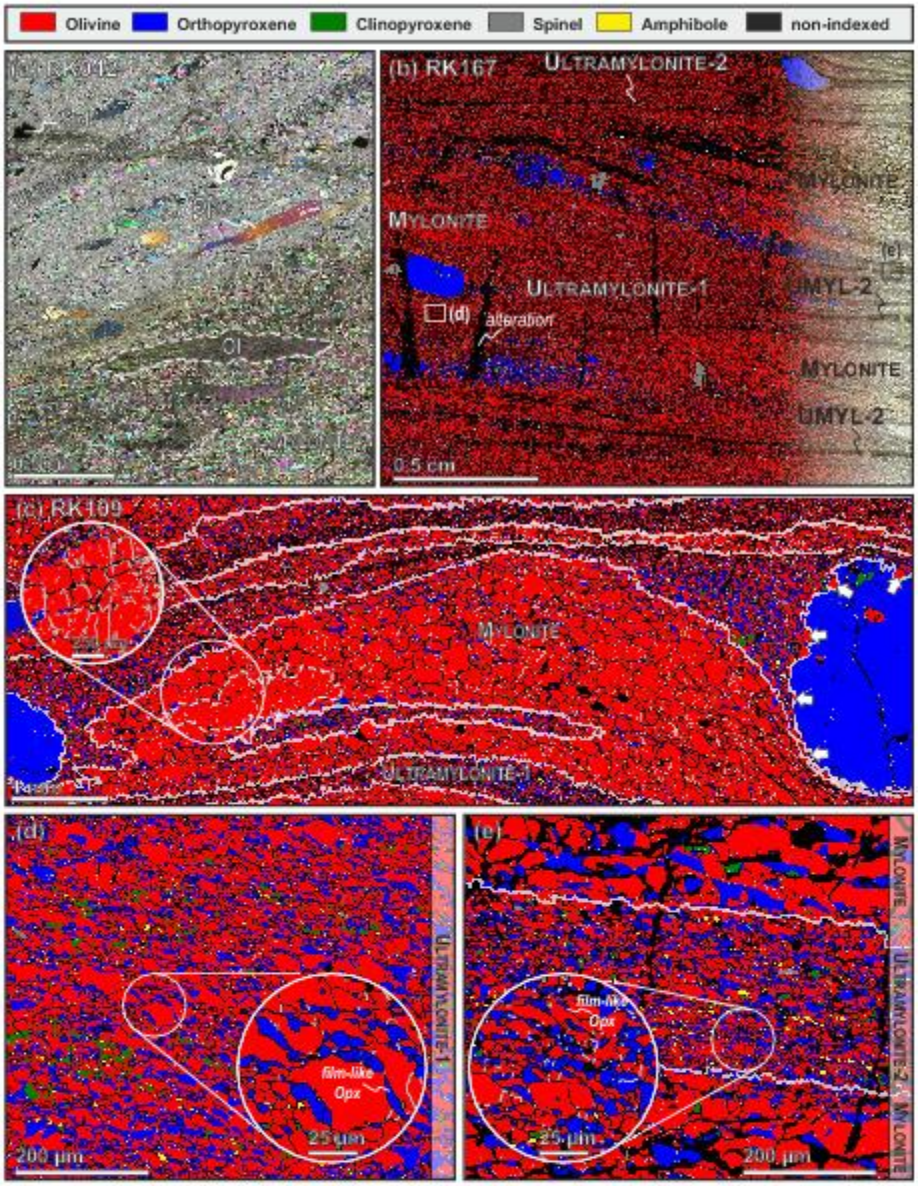

Fig. 5 Hidas et al.

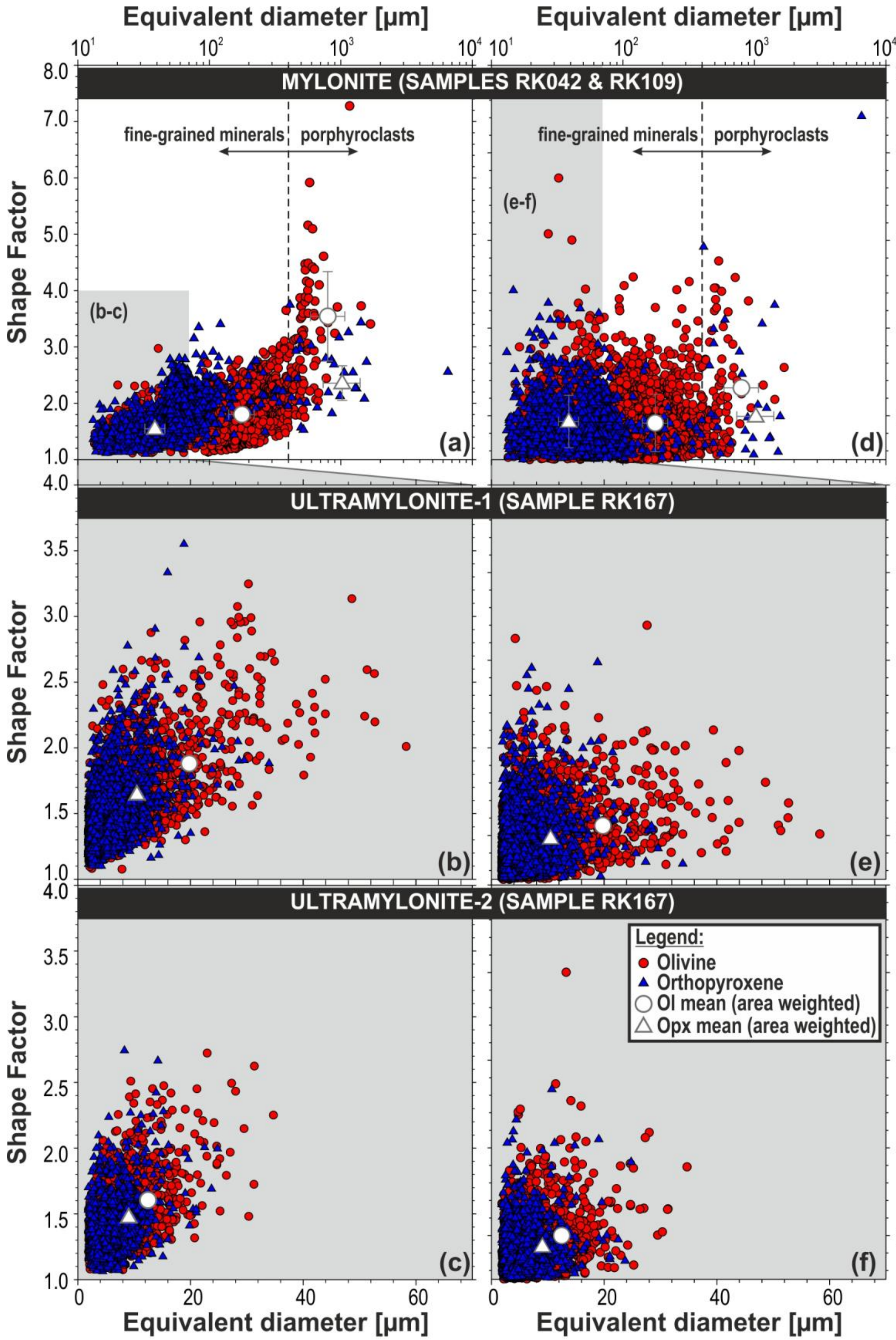

Fig. 6 Hidas et al.

ACCEPTED MANUSCRIPT

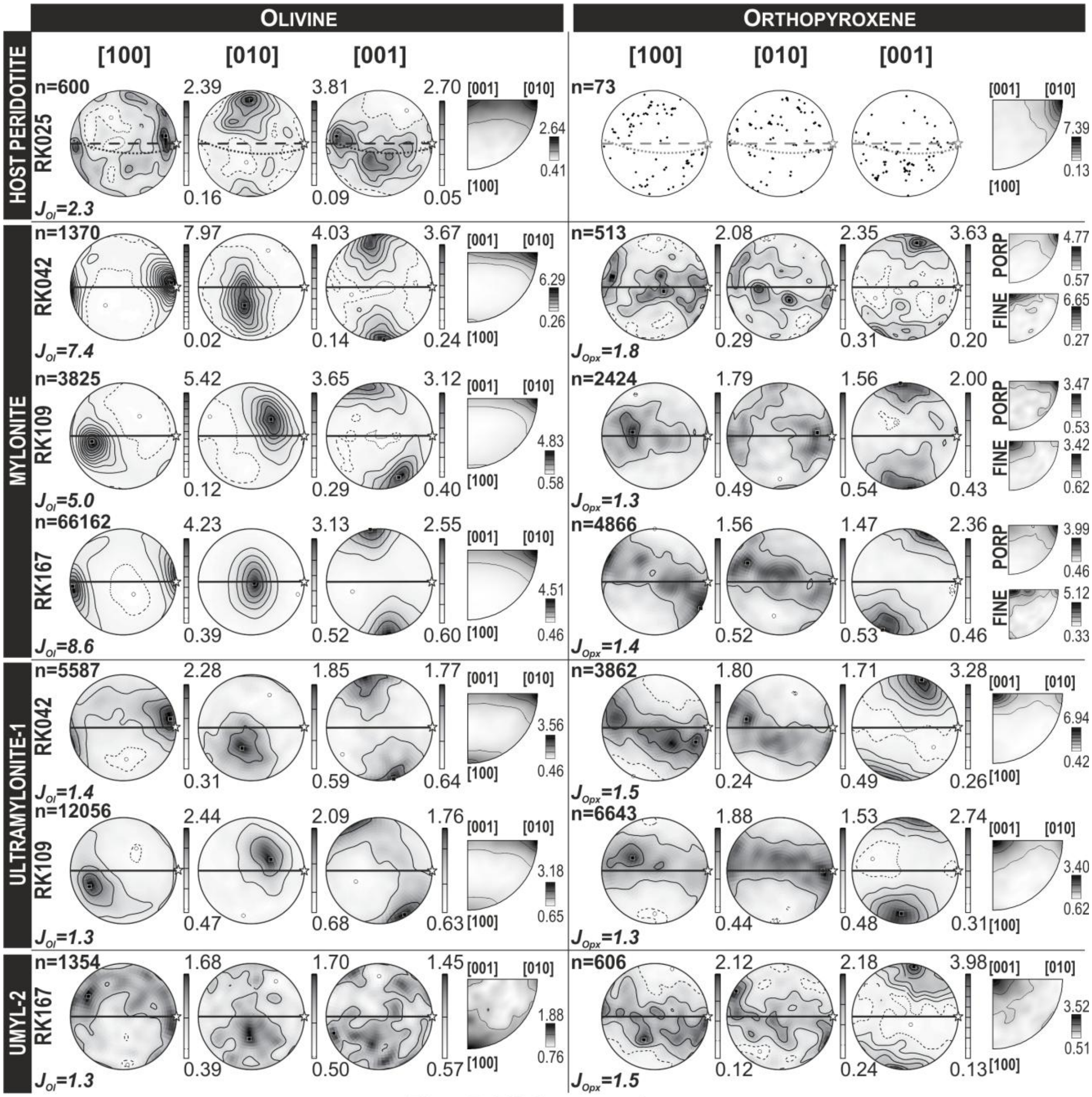

Fig. 7 Hidas et al.

ACCEPTED MANUSCRIPT

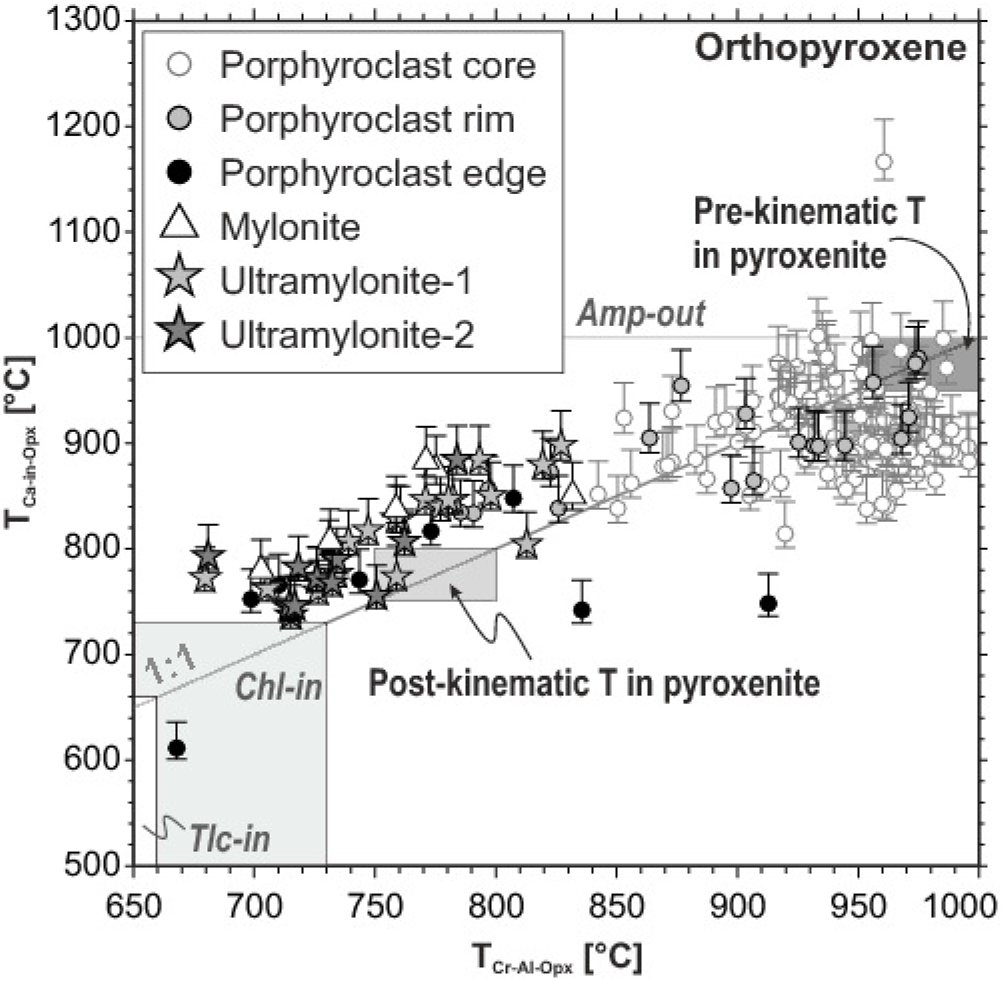

Fig. 8 Hidas et al.

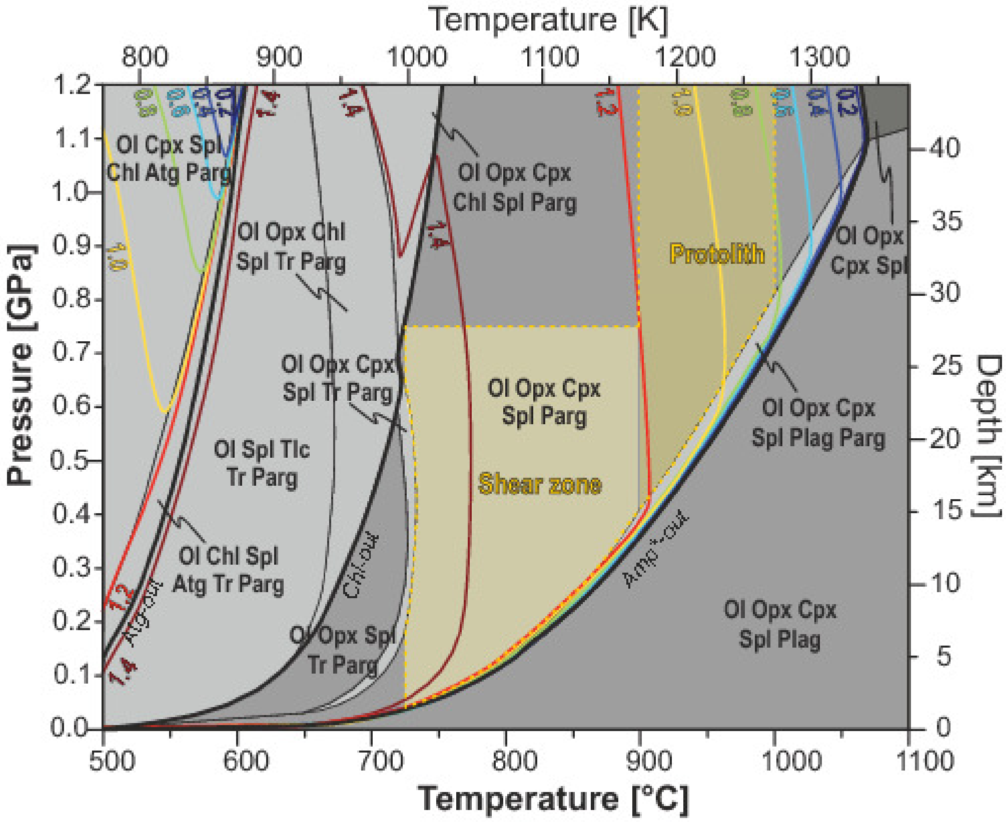

Fig. 9 Hidas et al.

ACCEPTED MANUSCRIPT

Table 1

	Protolith (WR)	Shear Zone (WR)		MYL (Domain)		UMYL-1 (Domain)	UMYL-2 (Domain)
Ol	74.8*	77.3*	76.2	81.6	(95.1)	73.8	75.2
Opx	23.3*	20.6*	21.6	17.9	(4.4)	23.2	21.4
Cpx	1.1*	0.8*	0.9	0.2	(0.2)	1.2	2.0
Spl	0.8*	1.3*	0.2	0.1	(0.1)	0.2	0.3
Amp	<0.5	1.2		0.2	(0.2)	1.6	1.0

Locality	Protolith whole rock			Shear zone whole rock			
Sample#	RK025	RK026	RK027	RK109	RK111B	RK111E	RK112
SiO_2	43.8	42.4	42.7	44.4	42.7	42.2	42.9
TiO_2	0.03	0.01	0.03	0.04	0.10	0.02	0.07
Al_2O_3	1.67	0.49	0.42	0.52	1.21	0.42	0.38
Cr_2O_3	0.37	0.41	0.39	0.35	0.40	0.33	0.34
FeO_t	7.58	8.12	7.68	7.52	7.62	7.29	7.30
MnO	0.14	0.13	0.13	0.13	0.13	0.13	0.13
MgO	41.9	45.0	45.5	44.9	42.5	43.2	44.8
NiO	0.28	0.29	0.30	0.30	0.28	0.29	0.30
CaO	1.74	0.51	0.36	0.43	1.16	0.36	0.36
Na_2O	<0.01	<0.01	<0.01	<0.01	<0.01	<0.01	<0.01
K_2O	<0.01	<0.01	<0.01	<0.01	<0.01	<0.01	<0.01
P_2O_5	0.02	0.01	0.01	0.01	0.02	0.01	0.01
LOI	2.42	2.67	1.96	0.41	3.03	4.80	2.79
Total	99.9	100.0	99.5	98.9	99.2	99.0	99.4
mg#	0.9079	0.9081	0.9135	0.9140	0.9086	0.9135	0.9163

ACCEPTED MANUSCRIPT

Highlights:

- Evidence for a feedback between fluid flow and strain localization in the shallow mantle
- Microstructural evidence for fluid-assisted dissolution-precipitation in peridotites
- Olivine CPO in mylonites indicates (001)[100] glide, probably in presence of fluids
- Evolution from dislocation creep to dissolution-precipitation by fluid focusing
- Abnormal orthopyroxene CPO interpreted as due to oriented crystallization